axioms

MDPI

Article

Improvement of the WENO-NIP Scheme for Hyperbolic Conservation Laws

Ruo Li [1,†] **and Wei Zhong** [2,3,*,†]

[1] CAPT, LMAM and School of Mathematical Sciences, Peking University, Beijing 100871, China; rli@math.pku.edu.cn
[2] School of Mathematical Sciences, Peking University, Beijing 100871, China
[3] Northwest Institute of Nuclear Technology, Xi'an 710024, China
* Correspondence: zhongwei2016@pku.edu.cn
† These authors contributed equally to this work.

Abstract: The WENO-NIP scheme was obtained by developing a class of L_1-norm smoothness indicators based on Newton interpolation polynomial. It recovers the optimal convergence order in smooth regions regardless of critical points and achieves better resolution than the classical WENO-JS scheme. However, the WENO-NIP scheme produces severe spurious oscillations when solving 1D linear advection problems with discontinuities at long output times, and it is also very oscillatory near discontinuities for 1D Riemann problems. In this paper, we find that the spectral property of WENO-NIP exhibits the negative dissipation characteristic, and this is the reason why WENO-NIP is unstable near discontinuities. Using this knowledge, we develop a way of improving the WENO-NIP scheme by introducing an additional term to eliminate the negative dissipation interval. The proposed scheme, denoted as WENO-NIP+, maintains the same convergence property, as well as the same low-dissipation property, as the corresponding WENO-NIP scheme. Numerical examples confirm that the proposed scheme is much more stable near discontinuities for 1D linear advection problems with large output times and 1D Riemann problems than the WENO-NIP scheme. Furthermore, the new scheme is far less dissipative in the region with high-frequency waves. In addition, the improved WENO-NIP+ scheme can remove or at least greatly decrease the post-shock oscillations that are commonly produced by the WENO-NIP scheme when simulating 2D Euler equations with strong shocks.

Keywords: hyperbolic problems; WENO; high order; high resolution; shock capturing scheme

MSC: 35L25; 35L35; 35L52; 35L65

Citation: Li, R.; Zhong, W. Improvement of the WENO-NIP Scheme for Hyperbolic Conservation Laws. *Axioms* **2022**, *11*, 190. https://doi.org/10.3390/axioms11050190

Academic Editor: Peixin Ye

Received: 3 March 2022
Accepted: 14 April 2022
Published: 20 April 2022

1. Introduction

Weighted essentially non-oscillatory (WENO) conservative schemes [1–12] have been studied widely since the 1990s for solving hyperbolic conservation laws, especially problems with both smooth fine-scale structures and discontinuities. Besides, the WENO schemes have also been widely used to solve other partial differential equations [13–16]. In addition, many WENO reconstructions that reconstruct entire polynomials, which can easily be evaluated and differentiated at any point instead of reconstructing point-values, have been proposed, and we refer to [17–20] for more details.

Liu et al. [1] devised the $(r+1)$th-order accurate WENO scheme, which was an improvement of the famous essentially non-oscillatory (ENO) schemes [21–24] and was the first WENO scheme. To improve the convergence order further, Jiang and Shu [2] developed the classical WENO scheme, dubbed WENO-JS, by proposing a new local smoothness indicator (LSI), which is a measurement of the smoothness of a solution over a particular substencil. As it can maintain the ENO property near discontinuities and achieve

the optimal convergence orders in most smooth regions, WENO-JS has become the most popular among the family of WENO schemes.

However, it was reported by Henrick et al. [10] that WENO-JS may fail to recover the optimal convergence rate of accuracy near critical points. To fix this issue, they proposed the first mapped WENO scheme, dubbed WENO-M, by introducing a mapping function to satisfy the sufficient condition for obtaining optimal convergence orders near critical points. Since then, a series of mapping functions have been designed [5–8,12,25,26] by obeying principles similar to WENO-M. It is well known [8,11,27] that most of the mapped WENO schemes suffer from expensive extra computational costs resulting from their complicated mapping procedures. A very different way of recovering the optimal convergence orders near critical points by WENO schemes is to use the higher-order information of the global stencil to construct the nonlinear weights. This idea was originally proposed by Borges et al. [11]. They introduced the global smoothness indicator (GSI) and hence devised the new nonlinear weights formula, which also satisfies the sufficient condition of optimal convergence. The resultant scheme was denoted as WENO-Z. If the power q of the weights of WENO-Z is set to be 2, the fifth-order WENO-Z scheme can achieve the optimal convergence orders regardless of critical points. In addition, as it is less dissipative, WENO-Z achieves better results than WENO-M. Moreover, the computational cost of WENO-Z is very cheap, and it is almost the same as that of WENO-JS. Inspired by the work of Borges et al. [11], many different WENO-Z-type schemes have been proposed by constructing different LSIs and GSIs.

Recently, Yuan [9] proposed a new WENO-Z-type scheme, dubbed WENO-NIP. Based on Newton interpolation polynomials, a class of smoothness indicators, including both LSI and GSI, was developed in the L_1 sense. One can easily check that the LSI of WENO-NIP is more succinct than that of the classical WENO-JS scheme. Yuan verified numerically that WENO-NIP can recover the fifth-order convergence rate of accuracy in smooth regions even in the presence of critical points. It was claimed [9] that WENO-NIP can resolve discontinuities sharply while keeping an essential non-oscillatory performance. However, closer examinations of solutions of the 1D Riemann problems used by Yuan (see Figures 4 and 5 of [9]) indicate that WENO-NIP produces evident spurious oscillations near discontinuities. In other words, WENO-NIP was unstable in some sense. Actually, our further calculations also show that WENO-NIP generates clear spurious oscillations (see examples in Section 4.3) and severe post-shock oscillations (see examples in Section 5.3) when solving 1D linear advection equation for long output times and 2D Euler equations with strong shock waves, respectively. In this paper, we try to analyze the reason why WENO-NIP suffers from these troubles and improve it accordingly.

The rest of the paper is organized as follows. In Section 2, the finite volume methodology and several different WENO schemes, including WENO-JS [2], WENO-Z [11], and WENO-NIP [9], are briefly described. In Section 3, we analyze the spectral property of WENO-NIP by using the ADR technique. The negative-dissipation interval of WENO-NIP will also be shown and discussed in this section. In Section 4, the design of the improved WENO-NIP scheme, termed WENO-NIP+, is proposed, as well as its basic properties and advantages for long-run simulations. Numerical experiments are conducted to demonstrate the enhancements of the proposed scheme in Section 5. Section 6 concludes this paper.

2. Brief Description of the WENO Schemes

In this section, we briefly describe the basic concepts of several fifth-order WENO schemes. Before that, we first review the finite volume methodology.

2.1. Finite Volume Methodology

For simplicity, we consider the one-dimensional hyperbolic conservation law

$$\frac{\partial u}{\partial t} + \frac{\partial}{\partial x} f(u) = 0, \quad x \in [x_l, x_r], t > 0, \tag{1}$$

with the initial condition $u(x,0) = u_0(x)$. For illustrative purposes in the present study, we consider the uniform meshes without loss of generality. Suppose that there are N uniform mesh cells, say, $I_j := [x_{j-1/2}, x_{j+1/2}], j = 1, \cdots, N$. The mesh size is $\Delta x = (x_r - x_l)/N$, the cell centers are $x_j = x_l + (j - 1/2)\Delta x$, and the cell boundaries are $x_{j\pm1/2} = x_j \pm \Delta x/2$. In numerical simulations, the objective is to calculate the approximations to the cell averages $\bar{u}(x_j,t) = \frac{1}{\Delta x}\int_{x_{j-1/2}}^{x_{j+1/2}} u(x,t)\mathrm{d}x$.

Taking I_j as the control volumes, the associated semi-discretization of Equation (1) can be reformulated as

$$\frac{\mathrm{d}\bar{u}_j(t)}{\mathrm{d}t} \approx -\frac{1}{\Delta x}\left(\hat{f}\left(u^-_{j+1/2}, u^+_{j+1/2}\right) - \hat{f}\left(u^-_{j-1/2}, u^+_{j-1/2}\right)\right), \tag{2}$$

where $\bar{u}_j(t)$ is the numerical approximation to $\bar{u}(x_j,t)$, and $\hat{f}\left(u^-_{j\pm1/2}, u^+_{j\pm1/2}\right)$ are the numerical fluxes, with $u^\pm_{j\pm1/2}$ referring to the limits of u at cell boundaries $x_{j\pm1/2}$. In this work, we compute $u^\pm_{j\pm1/2}$ by WENO reconstructions, as narrated later. The following global Lax–Friedrichs flux will be used in our calculations:

$$\hat{f}(a,b) = \frac{1}{2}[f(a) + f(b) - \alpha(b-a)],$$

where $\alpha = \max_u |f'(u)|$ is a constant, and the maximum is taken over the whole range of u.

Let

$$\mathcal{L}(u_j) = -\frac{1}{\Delta x}\left(\hat{f}\left(u^-_{j+1/2}, u^+_{j+1/2}\right) - \hat{f}\left(u^-_{j-1/2}, u^+_{j-1/2}\right)\right),$$

then, the semi-discretization scheme Equation (2) can be marched in time using a suitable time discretization method. In this paper, the following widely used third-order TVD Runge–Kutta method [28–30] is chosen:

$$\begin{cases} u_j^{(1)} = u_j^n + \Delta t\mathcal{L}(u_j^n), \\ u_j^{(2)} = \frac{3}{4}u_j^n + \frac{1}{4}u_j^{(1)} + \frac{1}{4}\Delta t\mathcal{L}(u_j^{(1)}), \\ u_j^{n+1} = \frac{1}{3}u_j^n + \frac{2}{3}u_j^{(2)} + \frac{2}{3}\Delta t\mathcal{L}(u_j^{(2)}), \end{cases}$$

where $u_j^{(i)}, i = 1,2$ are the intermediate stages, and u_j^n is the value of u at time level $t^n = n\Delta t$.

It should be noted that, instead of using Runge–Kutta technique for time integration, the ADER schemes (such as those proposed by Toro and Titarev [31–33]) could also be used. Readers may refer to [34–39] for more details.

2.2. Classical WENO-JS and WENO-Z Reconstructions

Taking $u^-_{j+1/2}$ as an example, we will review several classical WENO reconstruction procedures. For brevity of presentation but without causing any confusion, we drop the superscript "$-$" in the discussion below.

The fifth-order WENO reconstructions build $u_{j+1/2}$ through the convex combination of three ENO [21–24] reconstructions on three substencils, taking the form

$$u_{j+1/2} = \sum_{l=0}^{2} \omega_s u^s_{j+1/2}, \tag{3}$$

where $u^s_{j+1/2} = \sum_{l=0}^{2} c_{sl}\bar{u}_{j-s+l}$ with c_{sl} are the Lagrangian interpolation coefficients (see [2]), which depend on the parameter $s = 0,1,2$, but not on the values $\bar{u}_j$. Explicitly, we have

$$
\begin{aligned}
u^0_{j+1/2} &= \frac{1}{6}(2\bar{u}_{j-2} - 7\bar{u}_{j-1} + 11\bar{u}_j),\\
u^1_{j+1/2} &= \frac{1}{6}(-\bar{u}_{j-1} + 5\bar{u}_j + 2\bar{u}_{j+1}),\\
u^2_{j+1/2} &= \frac{1}{6}(2\bar{u}_j + 5\bar{u}_{j+1} - \bar{u}_{j+2}).
\end{aligned} \tag{4}
$$

For the classical WENO-JS scheme [2], the nonlinear weights are computed by

$$
\omega_s^{\mathrm{JS}} = \frac{\alpha_s^{\mathrm{JS}}}{\sum_{l=0}^{2} \alpha_l^{\mathrm{JS}}}, \quad \alpha_s^{\mathrm{JS}} = \frac{d_s}{(\beta_s + \epsilon)^2}, \tag{5}
$$

where β_s are the local smoothness indicators, and ϵ is a very small positive real number introduced to prevent the denominator from becoming 0. For the fifth-order WENO-JS scheme, the explicit formulae of β_s in terms of the cell-averaged value of u are as follows:

$$
\begin{aligned}
\beta_0 &= \frac{13}{12}\left(\bar{u}_{j-2} - 2\bar{u}_{j-1} + \bar{u}_j\right)^2 + \frac{1}{4}\left(\bar{u}_{j-2} - 4\bar{u}_{j-1} + 3\bar{u}_j\right)^2,\\
\beta_1 &= \frac{13}{12}\left(\bar{u}_{j-1} - 2\bar{u}_j + \bar{u}_{j+1}\right)^2 + \frac{1}{4}\left(\bar{u}_{j-1} - \bar{u}_{j+1}\right)^2,\\
\beta_2 &= \frac{13}{12}\left(\bar{u}_j - 2\bar{u}_{j+1} + \bar{u}_{j+2}\right)^2 + \frac{1}{4}\left(3\bar{u}_j - 4\bar{u}_{j+1} + \bar{u}_{j+2}\right)^2.
\end{aligned} \tag{6}
$$

It was reported that WENO-JS was only third-order convergence order near critical points [10], and it was too dissipative. To recover the optimal convergence orders, Borges et al. [11] developed the classical WENO-Z scheme by introducing a higher-order global smoothness indicator, say, $\tau = |\beta_2 - \beta_0|$, resulting in the following nonlinear weights formula:

$$
\omega_s^{\mathrm{Z}} = \frac{\alpha_s^{\mathrm{Z}}}{\sum_{l=0}^{2} \alpha_l^{\mathrm{Z}}}, \quad \alpha_s^{\mathrm{Z}} = d_s\left(1 + \left(\frac{\tau}{\beta_s + \epsilon}\right)^2\right). \tag{7}
$$

It is well known that τ measures the smoothness of the global stencil. Thus, WENO-Z is less dissipative than WENO-JS, as it assigns larger weights to the less smooth substencils. Furthermore, if taking $p = 2$, WENO-Z can recover the fifth-order convergence rate of accuracy even at critical points.

2.3. The WENO-NIP Reconstruction

Yuan [9] constructs a new local smoothness indicator by using Newton interpolation polynomials based on L_1 norm. The new local smoothness indicator for the fifth-order scheme was defined as

$$
\chi_s = \theta|\Delta x N_s^{(1)}(x_{j+1/2})| + |\Delta x^2 N_s^{(2)}(x_{j+1/2})|,
$$

where θ is a parameter that governs the trade-off between the accuracies around the smooth regions and discontinuous regions, and $N_s^{(i)}, i = 1, 2$ is the ith-order derivative of a Newton interpolation polynomial, which was defined carefully in [9]. For more details, we refer readers to the reference. Here, we decide to explicitly state these local smoothness indicators as follows:

$$
\begin{aligned}
\chi_0 &= \theta\left|\bar{u}_{j-2} - 3\bar{u}_{j-1} + 2\bar{u}_j\right| + \left|\bar{u}_{j-2} - 2\bar{u}_{j-1} + \bar{u}_j\right|,\\
\chi_1 &= \theta\left|\bar{u}_{j+1} - \bar{u}_j\right| + \left|\bar{u}_{j-1} - 2\bar{u}_j + \bar{u}_{j+1}\right|,\\
\chi_2 &= \theta\left|\bar{u}_{j+1} - \bar{u}_j\right| + \left|\bar{u}_j - 2\bar{u}_{j+1} + \bar{u}_{j+2}\right|.
\end{aligned}
$$

In [9], $\theta = 0.1$ was recommended.

The nonlinear weights for the WENO-NIP scheme are defined as

$$\omega_s^{\mathrm{NIP}} = \frac{\alpha_s^{\mathrm{NIP}}}{\sum_{l=0}^{2} \alpha_l^{\mathrm{NIP}}},$$

with

$$\alpha_s^{\mathrm{NIP}} = d_s\left(1 + \frac{\tau^{\mathrm{NIP}}}{(\chi_s + \epsilon)^2}\right), \tag{8}$$

where τ^{NIP} is the global smoothness indicator of WENO-NIP, and it was defined as $\tau^{\mathrm{NIP}} = \left|\bar{u}_{j-2} - 4\bar{u}_{j-1} + 6\bar{u}_j - 4\bar{u}_{j+1} + \bar{u}_{j+2}\right|^J$. In [9], $J = 2.0$ was recommended.

3. Analysis of the WENO-NIP Scheme

In this section, we analyze the dispersion and dissipation properties of WENO-NIP. It is well known that, for a nonlinear scheme, there is no analytical formula for the spectral relations. However, the spectral properties of the nonlinear scheme can be analyzed by using the approximate dispersion relation (ADR) proposed by Pirozzoli [40].

The ADR is the relationship between the reduced wavenumber φ and the modified wavenumber $\Phi(\varphi)$, which can be computed by the technique of Pirozzoli [40]. Note that $\Phi(\varphi)$ is a complex number, and its real part and imaginary part indicate the dispersion property and the dissipation property of the nonlinear scheme, respectively.

In Figure 1, we plot the main results of the WENO-NIP scheme using the ADR method [40] in terms of the real and the imaginary part of the modified wavenumber $\Phi(\varphi)$. We focus our attention on the dissipation property of the WENO-NIP scheme as shown in Figure 1b. It can be seen that the WENO-NIP scheme causes negative dissipation, say, $\mathrm{Im}(\Phi(\varphi)) > 0$ for wave components within a certain wavenumber interval. In other words, the WENO-NIP scheme enjoys very low dissipation. This finding can be used to explain why the WENO-NIP scheme generates greatly improved results in some numerical test cases. However, the low dissipation also significantly increases the risk of instability. Indeed, as mentioned before, WENO-NIP generates clear spurious oscillations near discontinuities when solving 1D linear advection equations and 1D Riemann problems. In this sense, the goal of this paper is to eliminate the negative dissipation to improve the stability and other performances of the WENO-NIP scheme.

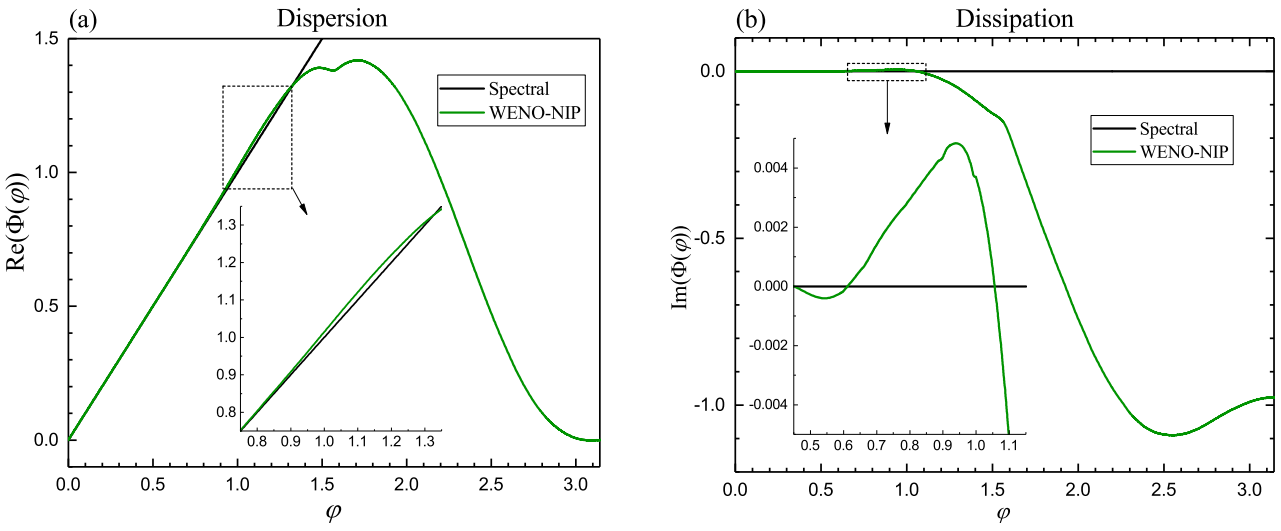

Figure 1. (**a**) The dispersion properties of WENO-NIP. (**b**) The dissipation properties of WENO-NIP.

4. The Improved WENO-NIP Scheme

4.1. The Improved Nonlinear Weights

Now, we try to improve the WENO-NIP scheme by eliminating its negative dissipation characteristic. The idea is to add a new term to the WENO-NIP non-normalized nonlinear weights formula Equation (8), resulting in the following formula:

$$\alpha_s^{\mathrm{NIP}+} = d_s\left(1 + \frac{\tau^{\mathrm{NIP}}}{(\chi_s+\epsilon)^2} + \zeta_s^{\mathrm{NIP}+}\right). \tag{9}$$

The additional term $\zeta_s^{\mathrm{NIP}+}$ should be able to remove the negative-dissipation interval of WENO-NIP. After extensive numerical experiments, we find a simple way of defining such a $\zeta_s^{\mathrm{NIP}+}$, as follows:

$$\zeta_s^{\mathrm{NIP}+} = \frac{1-\mu}{(\chi_s+\epsilon)^2}\left(\left(\frac{\chi_s+\epsilon}{\beta_s+\epsilon}\right)^2 - (\chi_s+\epsilon)^2 - \tau^{\mathrm{NIP}}\right), \tag{10}$$

where β_s is computed by Equation (6), and μ is defined by

$$\mu = \begin{cases} 1, & \text{if} \quad \kappa > 0, \\ 0, & \text{otherwise}, \end{cases} \tag{11}$$

with

$$\kappa = \min_{\substack{0\le m,n\le 2 \\ m\neq n}} \lambda(m,n), \quad \lambda(m,n) = \left(\omega_m^{\mathrm{JS}} - \omega_n^{\mathrm{JS}}\right)\left(\omega_m^{\mathrm{NIP}} - \omega_n^{\mathrm{NIP}}\right).$$

Finally, we obtain the improved nonlinear weights

$$\omega_s^{\mathrm{NIP}+} = \frac{\alpha_s^{\mathrm{NIP}+}}{\sum_{l=0}^{2}\alpha_l^{\mathrm{NIP}+}}. \tag{12}$$

The associated improved scheme is denoted as WENO-NIP+.

Thus far, introducing the additional term seems to be an empirical treatment. However, the ADR analysis below will confirm that it indeed satisfies our requirement of removing the negative-dissipation interval of WENO-NIP. Moreover, extensive numerical tests will demonstrate that this modification brings about the desired improvement of removing spurious oscillations and other remarkable enhancements in many aspects.

4.2. The ADR Analysis

In this subsection, we study the spectral properties of the WENO-NIP+ scheme. For comparison purposes, we also consider the spectral properties of the WENO-NIP, WENO-JS, WENO-Z, and the fifth-order upwind (UW5) schemes. As before, we perform ADR analysis of these considered WENO schemes, since the ADR reveals the numerical performance of the scheme in the whole wavenumber space.

Figure 2 shows the ADR of the WENO-NIP+ scheme and its associated WENO-NIP scheme, as well as the WENO-JS, WENO-Z, and UW5 schemes. As expected, the dispersion and dissipation of WENO-NIP+ are smaller than that of WENO-JS.

We pay special attention to the dissipation property of WENO-NIP+ given in Figure 2b. Obviously, WENO-NIP+ has successfully eliminated the negative-dissipation interval, which is about $\varphi \in (0.619, 1.056)$, observed in the results of WENO-NIP. In the region of low reduced wavenumbers of $\varphi < 1.216$, as well as the region of high reduced wavenumbers of $\varphi > 1.8$, the dissipation of WENO-NIP+ is smaller than that of WENO-Z. Therefore, the WENO-NIP+ scheme is less dissipative than the WENO-Z scheme. Indeed, in the region of low reduced wavenumbers of $\varphi < 1.216$, the dissipation of WENO-NIP+ is even smaller than that of UW5. It should be noted that the dissipation property of the ADR of WENO-NIP+ is inferior to those of WENO-NIP and UW5 in the region of medium and high

reduced wavenumbers. However, WENO-NIP and UW5 are unstable near discontinuities where WENO-NIP+ is much more stable. This fact indicates that the anti-dissipation of WENO-NIP+ is helpful to avoid spurious oscillations for discontinuous solutions.

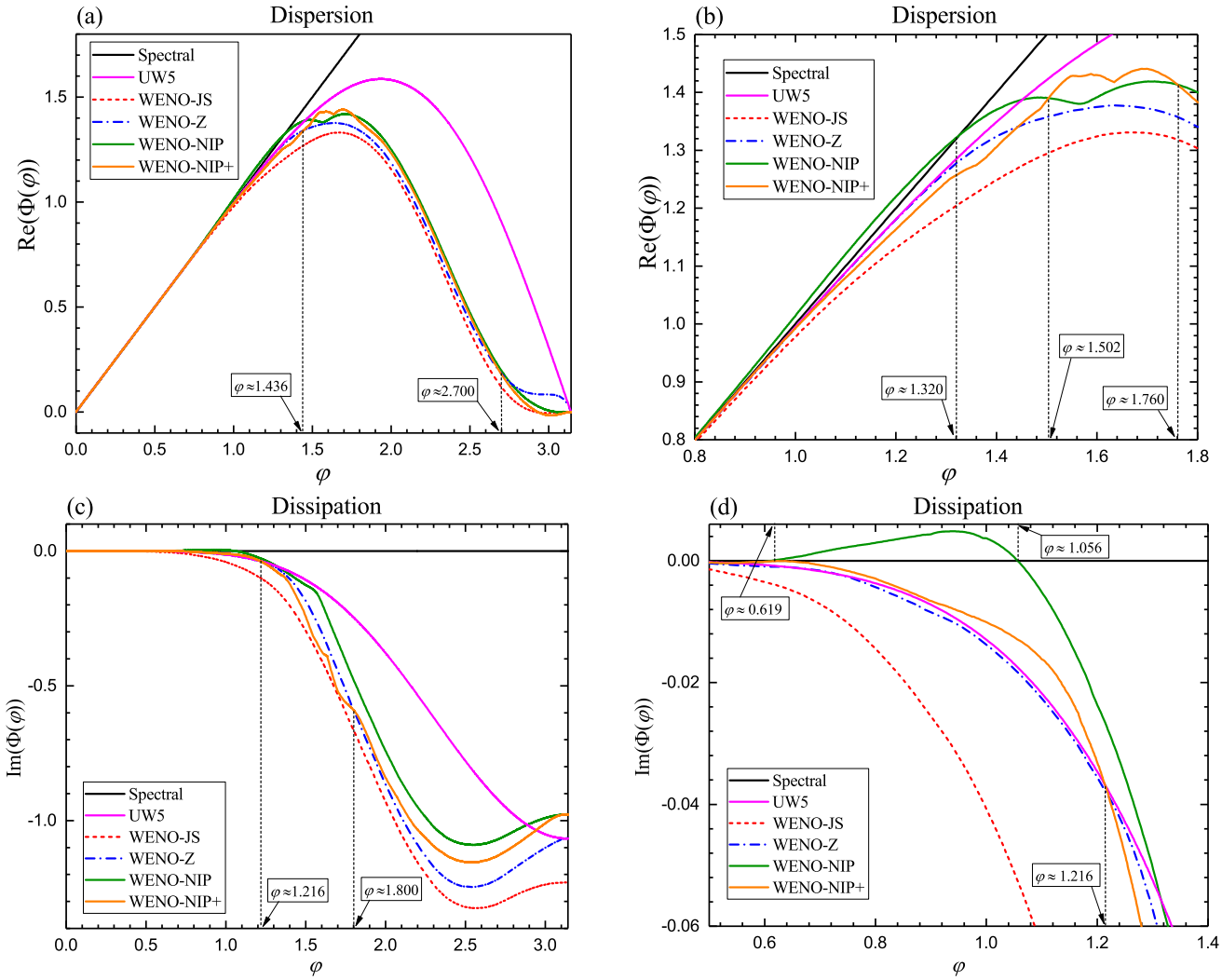

Figure 2. (**a**) Comparison of the dispersion properties of different schemes. (**b**) Zoomed-in view of (**a**). (**c**) Comparison of the dissipation properties of different schemes. (**d**) Zoomed-in view of (**c**).

4.3. Long-Run Simulations of the 1D Linear Advection Equation

To demonstrate the competitive advantage of the proposed WENO-NIP+ scheme, and that it is able to attain high resolutions and prevent spurious oscillations for long-run calculations, we solve the following standard 1D linear advection equation:

$$\begin{cases} u_t + u_x = 0, & x \in (x_{\mathrm{L}}, x_{\mathrm{R}}), \\ u(x,0) = u_0(x), \end{cases}$$

with two different initial conditions. For all tests in this subsection, the CFL number is set as 0.1.

4.3.1. The Gaussian-Square-Triangle-Ellipse Linear Test

Example 1. *In the first example, we solve the widely used Gaussian-square-triangle-ellipse test proposed in [2]. The computational domain is* $(x_{\mathrm{L}}, x_{\mathrm{R}}) = (-1, 1)$*, and it is initialized by*

$$u_0(x) = \begin{cases} \frac{1}{6}\left[G(x,\beta,z-\hat{\delta}) + 4G(x,\beta,z) + G(x,\beta,z+\hat{\delta})\right], & x \in [-0.8,-0.6], \\ 1, & x \in [-0.4,-0.2], \\ 1 - \left|10(x-0.1)\right|, & x \in [0.0,0.2], \\ \frac{1}{6}\left[F(x,\alpha,a-\hat{\delta}) + 4F(x,\alpha,a) + F(x,\alpha,a+\hat{\delta})\right], & x \in [0.4,0.6], \\ 0, & \text{otherwise}, \end{cases}$$

where $G(x,\beta,z) = \mathrm{e}^{-\beta(x-z)^2}, F(x,\alpha,a) = \sqrt{\max\left(1-\alpha^2(x-a)^2,0\right)}$, *and the constants are* $z = -0.7, \hat{\delta} = 0.005, \beta = \frac{\log 2}{36\hat{\delta}^2}, a = 0.5$, *and* $\alpha = 10$. *The periodic boundary conditions are used at* $x = \pm 1$.

The solutions of WENO-NIP+ and its associated WENO-NIP, as well as WENO-JS and WENO-Z, at $t = 2000$ (1000 cycles) for $N = 800$ are plotted in Figure 3. Clearly, WENO-NIP generates severe spurious oscillations, while WENO-NIP+ can avoid these oscillations. Moreover, WENO-NIP+ can attain considerably high resolution. Actually, its resolution is noticeably improved compared to that of WENO-Z and much higher than that of WENO-JS.

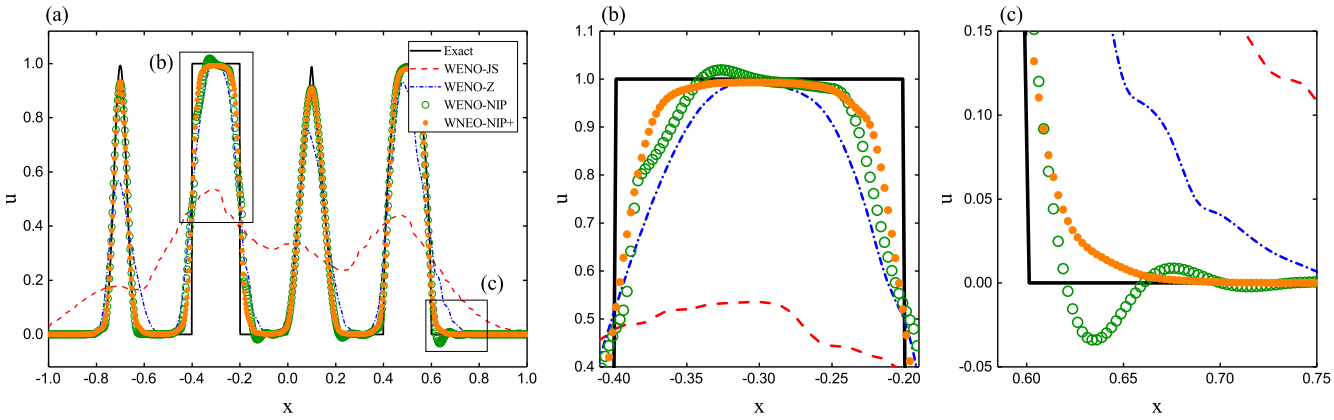

Figure 3. (**a**) Results of the Gaussian-square-triangle-ellipse linear test with $t = 2000$ (1000 cycles) and $N = 800$. (**b**) Zoomed-in view of the top of the square wave. (**c**) Zoomed-in view of right bottom of the ellipse wave.

We also calculate this problem using refined meshes of $N = 1600$ and $N = 3200$ with a shortened but still large output time of $t = 200$ (100 cycles). The results are plotted in Figure 4 and Figure 5, respectively. As expected, WENO-NIP+ obtains better resolutions than WENO-Z and WENO-JS, and it can still prevent spurious oscillations regardless of the meshes. However, WENO-NIP produces evident spurious oscillations.

4.3.2. The Modified Linear Test

Example 2. *To further explain the advantage of WENO-NIP+ on long-run simulations, in this example, we solve a modified version of the Gaussian-square-triangle-ellipse test. This is a more complicated test, and we call it ZWACM for brevity in the discussion. Let* $\Omega_0 = [-1.25,-1.2] \bigcup (-0.9,0.6] \bigcup (-0.1,-0.06] \bigcup (0.2,0.25] \bigcup (0.75,0.8] \bigcup (1.2,1.25]$, $\Omega_1 = (-1.2,-0.9] \bigcup (-0.6,-0.55] \bigcup (-0.15,-0.1]$; *then, the computational domain* $(x_{\mathrm{L}}, x_{\mathrm{R}}) = (-1.25,1.25)$ *is initialized by*

$$u(x,0) = \begin{cases} 0, & x \in \Omega_0, \\ 1 - \left|10(x+0.55)\right|, & x \in (-0.55, -0.45], \\ 1 - \left|10(x+0.35)\right|, & x \in (-0.45, -0.25], \\ 1 - \left|10(x+0.15)\right|, & x \in (-0.25, -0.15], \\ \frac{1}{6}\left[G(x,\beta,z-\hat{\delta}) + 4G(x,\beta,z) + G(x,\beta,z+\hat{\delta})\right], & x \in [-0.06, 0.2], \\ \frac{1}{6}\left[F(x,\alpha,a-\hat{\delta}) + 4F(x,\alpha,a) + F(x,\alpha,a+\hat{\delta})\right], & x \in [0.25, 0.75], \\ 1 - \left|10(x-0.9)\right|, & x \in (0.8, 1.0], \\ 1 - \left|10(x-1.1)\right|, & x \in (1.0, 1.2], \\ 1, & x \in \Omega_1, \end{cases}$$

where the functions $G(x,\beta,z), F(x,\alpha,a)$ *and the constants* $z, \hat{\delta}, \beta, a, \alpha$ *are the same as given in Example 1. The periodic boundary conditions are used at* $x = \pm 1.25$.

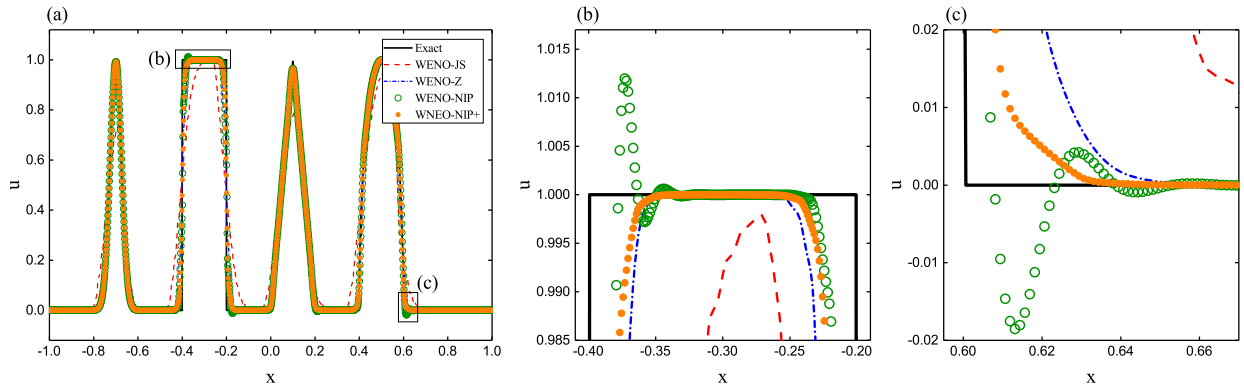

Figure 4. (**a**) Results of the Gaussian-square-triangle-ellipse linear test with $t = 200$ (100 cycles) and $N = 1600$. (**b**) Zoomed-in view of the top of the square wave. (**c**) Zoomed-in view of right bottom of the ellipse wave.

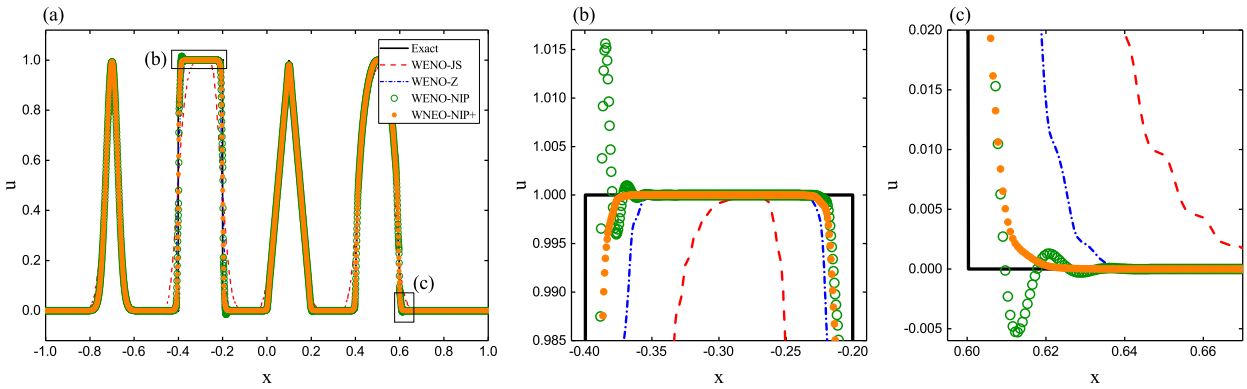

Figure 5. (**a**) Results of the Gaussian-square-triangle-ellipse linear test with $t = 200$ (100 cycles) and $N = 3200$. (**b**) Zoomed-in view of the top of the square wave. (**c**) Zoomed-in view of right bottom of the ellipse wave.

Figure 6 presents the solutions of WENO-NIP+ and its associated WENO-NIP, as well as WENO-JS and WENO-Z, at $t = 2500$ (1000 cycles) for $N = 800$. As before, we can observe that WENO-NIP generates severe spurious oscillations. However, these spurious oscillations have been removed in the results of WENO-NIP+. Moreover, it is clear that the resolution of WENO-NIP+ is greatly improved compared to that of WENO-Z, and of course, it is much higher than that of WENO-JS. Besides, the resolution of WENO-NIP+ is even better than that of WENO-NIP in some special regions, as shown in Figure 6c.

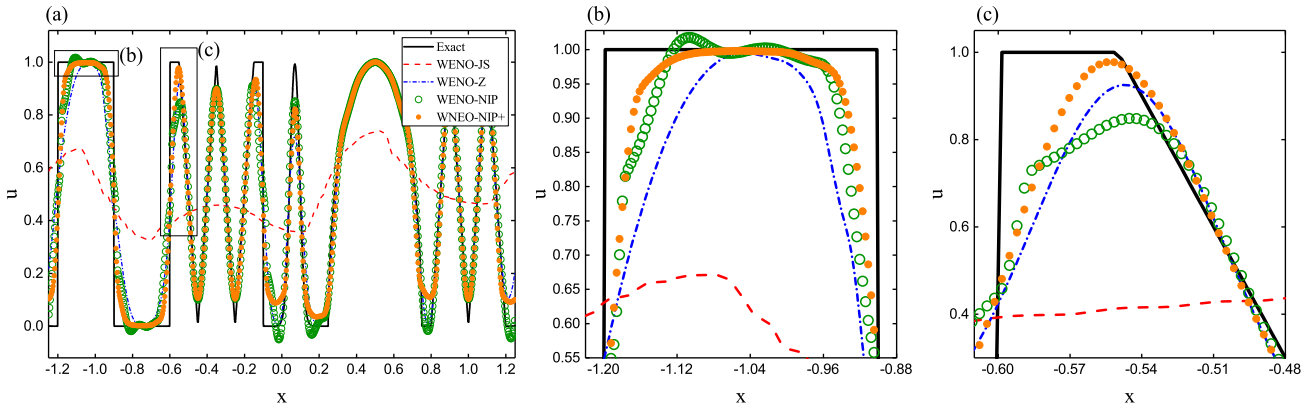

Figure 6. (**a**) Results of the ZWACM linear test with $t = 2500$ (1000 cycles) and $N = 800$. (**b**) Zoomed-in view of the top of the square wave. (**c**) Zoomed-in view of the concerned region as marked in (**a**).

Similarly, we also compute this problem using refined meshes of $N = 1600$ and $N = 3200$ with a shortened but still large output time of $t = 200$ (80 cycles). In Figures 7 and 8, we plot the solutions of the considered schemes. As expected, WENO-JS gives the lowest resolutions among all considered schemes due to its largest dissipation. The resolution of WENO-NIP appears to be very high, while WENO-NIP also produces unfavorable spurious oscillations. It is clear that WENO-NIP+ achieves considerably high resolutions which are better than those of WENO-Z. Most importantly, WENO-NIP+ can successfully remove the spurious oscillations of WENO-NIP.

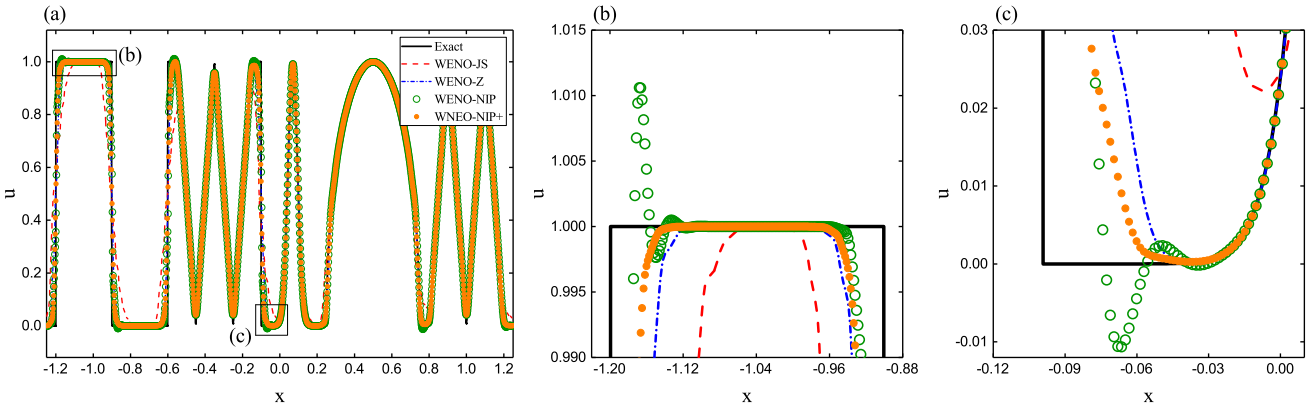

Figure 7. (**a**) Results of the ZWACM linear test with $t = 200$ (80 cycles) and $N = 1600$. (**b**) Zoomed-in view of the top of the square wave. (**c**) Zoomed-in view of the concerned region as marked in (**a**).

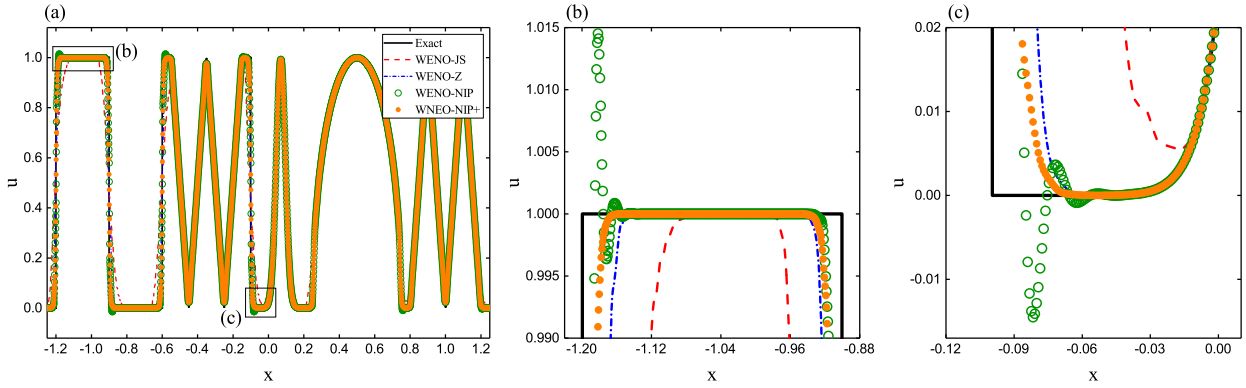

Figure 8. (**a**) Results of the ZWACM linear test with $t = 200$ (80 cycles) and $N = 3200$. (**b**) Zoomed-in view of the top of the square wave. (**c**) Zoomed-in view of the concerned region as marked in (**a**).

To summarize, we can conclude that the improved WENO-NIP+ scheme can achieve considerably high resolutions on the premise of preventing spurious oscillations for long-run simulations of problems with discontinuities.

4.3.3. Comparison with the CWENO Schemes

Next, we compare the behavior of the WENO-NIP+ scheme with the CWENO schemes (central WENO approaches). The well-validated WENO-NW6 [41], WENO-CU6 [42], and WENO-θ6 [43] schemes are considered in the present work.

Example 3. *Firstly, we solve the following problem with periodic boundary conditions.*

$$\begin{cases} u_t + u_x = 0, & x \in (-1, 1), \\ u(x, 0) = \max(-\sin(\pi x), 0). \end{cases} \tag{13}$$

The solutions are advanced to $t = 2.4$ *with a uniform mesh size of* $N = 200$.

Figure 9 shows the solutions of this problem computed by the sixth-order central schemes of WENO-NW6, WENO-CU6, and WENO-θ6 and the proposed WENO-NIP+ scheme. For comparison purposes, we also plot the results of the WENO-JS, WENO-Z, and WENO-NIP schemes. From Figure 9, we can see that the WENO-NIP+ scheme, as well as the WENO-JS, WENO-Z, and WENO-NIP schemes, outperforms the sixth-order central WENO schemes of WENO-NW6 and WENO-CU6 on resolution. As indicated by Jung et al. [43], the loss of resolution from the results of the WENO-NW6 and WENO-CU6 schemes is an important issue, since there are many problems whose solution often exhibits the same behavior as this example. In other words, we can conclude that the proposed WENO-NIP+ scheme is more favorable than the sixth-order central WENO schemes of WENO-NW6 and WENO-CU6 for this kind of problem. It should be pointed out that the the central WENO scheme of WENO-θ6 gives comparable results to the WENO-NIP+ scheme. Of course, this is good for this test. However, we find that it presents greatly lower resolution than the WENO-NIP+ scheme when simulating problems with discontinuities at long output times.

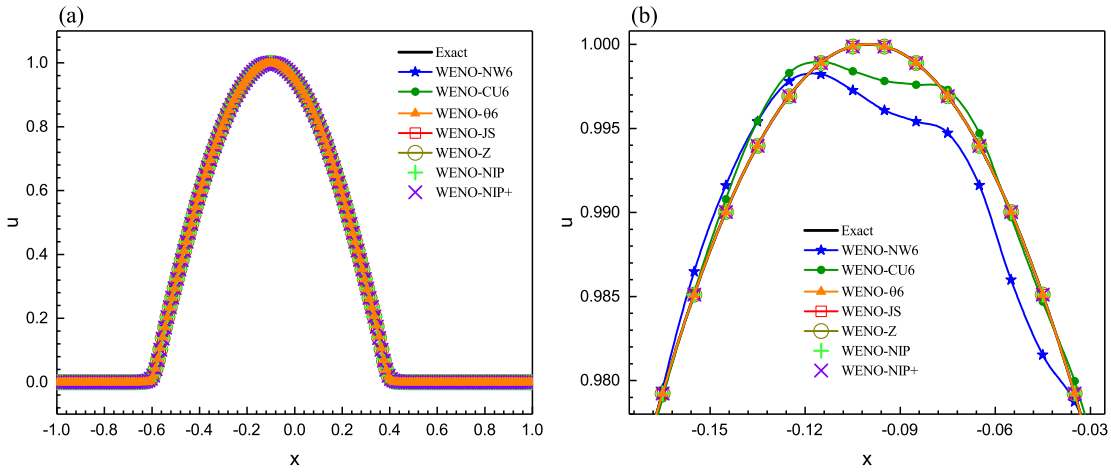

Figure 9. (**a**) Numerical solutions of Equation (13) at time $t = 2.4$ computed by different WENO schemes. (**b**) Zoom near the critical region.

Taking the previously used Gaussian-square-triangle-ellipse linear test (see Example 1) as an example, we now further compare the behavior of the WENO-NIP+ scheme with the WENO-NW6, WENO-CU6, and WENO-θ6 schemes.

Figure 10 plots the solutions of the Gaussian-square-triangle-ellipse linear test solved by the sixth-order central schemes of WENO-NW6, WENO-CU6, and WENO-θ6, as well as the WENO-NIP and WENO-NIP+ schemes, with a uniform mesh size of $N = 3200$ at $t = 200$.

As expected, Figure 10 shows that the resolutions of the WENO-NW6 and WENO-θ6 schemes are much lower than that of the WENO-NIP+ scheme in general. Although the resolution of the WENO-CU6 scheme appears to be equivalent to, or even better than, that of the WENO-NIP+ scheme in most regions, it produces evident spurious oscillations. Clearly, the WENO-NIP+ scheme can successfully avoid these spurious oscillations. In addition, as shown in Figure 10e, the resolution of the WENO-CU6 scheme is also lower than that of the WENO-NIP+ scheme on the top of the ellipse wave.

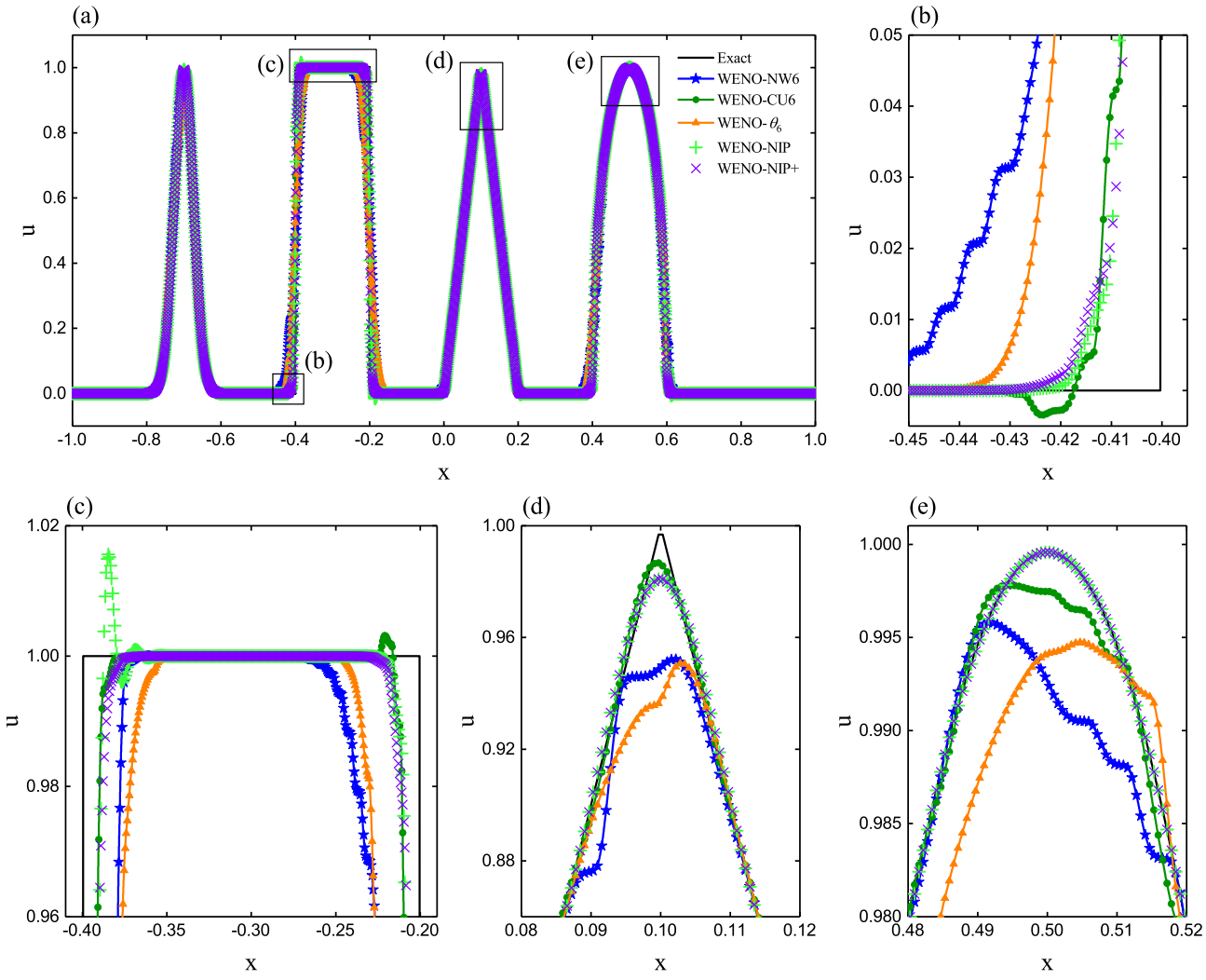

Figure 10. (**a**) Results of the Gaussian-square-triangle-ellipse linear test (see Example 1) computed by the WENO-NW6, WENO-CU6, WENO-θ6, WENO-NIP, and WENO-NIP+ schemes with $t = 200$ and $N = 3200$. (**b**) Zoomed in view of the left bottom of the square wave. (**c**) Zoomed in view of the top of the square wave. (**d**) Zoomed in view of the top of the triangle wave. (**e**) Zoomed in view of the top of the ellipse wave.

5. Numerical Results

Now, we conduct numerical experiments to demonstrate the enhancements of the proposed WENO-NIP+ scheme. For the purpose of comparison, we also present the numerical results of the WENO-JS, WENO-Z, and WENO-NIP schemes. Unless otherwise noted, the CFL number will be set as 0.5, and for the Euler systems, we use the decomposition through the local characteristic variables [2]. All WENO schemes are applied dimension by dimension to solve 2D problems together with the third Runge–Kutta methods.

5.1. Accuracy Test

Example 4. *In order to verify that the proposed WENO-NIP+ scheme is indeed fifth-order accurate in space and time, the "oblique" linear advection problem [44] with the following initial condition is computed:*

$$\begin{cases} \dfrac{\partial C}{\partial t} + \dfrac{\partial C}{\partial x} + \dfrac{\partial C}{\partial y} = 0, & (x,y) \in [0,1] \times [0,1], t > 0, \\ C_0(x,y) = \sin\Big(2\pi(x+y)\Big), & (x,y) \in [0,1] \times [0,1], t = 0. \end{cases} \tag{14}$$

The periodic boundary condition is used. Denote $h = h_x = h_y$*, and the CFL number is taken to be* $h^{2/3}$*. It is trivial to know that the exact solution to Equation* (14) *is simply* $C(x,y,t) = \sin\Big(2\pi\big(x+y-2t\big)\Big)$.

In Table 1, we give the L_2- and L_∞-norm accuracy and orders of convergence of the WENO-JS, WENO-Z, WENO-NIP, and WENO-NIP+ schemes with a final time of $t = 2.0$. As displayed in Table 1, all schemes achieve the fifth-order convergence orders. As expected, WENO-JS generates the largest numerical errors. Most importantly, the numerical errors of WENO-NIP+ are identical to those of WENO-NIP. Figure 11 shows the overall L_2 and L_∞ convergence behavior of different schemes. From Figure 11, we can intuitively see that the solutions of all the considered schemes converge at the optimal order, as evidenced by the slopes of the lines, especially for slightly larger grid numbers.

We examine the CPU time consumed by different considered schemes for this test. Figure 12 plots the graphs for the CPU time versus the L_2- and L_∞-norm computing errors. It can be seen that the WENO-NIP+ scheme has much better efficiency than the WENO-JS scheme, although it consumes more CPU time than the WENO-Z and WENO-NIP schemes.

Table 1. Numerical errors and convergence orders of accuracy when solving Example 4, $t = 2.0$, CFL = $h^{2/3}$.

	WENO-JS				**WENO-Z**			
$N_x \times N_y$	L_2 **Error**	L_2 **Order**	L_∞ **Error**	L_∞ **Order**	L_2 **Error**	L_2 **Order**	L_∞ **Error**	L_∞ **Order**
32×32	9.14867×10^{-4}	-	1.30212×10^{-3}	-	1.37189×10^{-4}	-	1.93670×10^{-4}	-
64×64	2.89801×10^{-5}	4.9804	4.60009×10^{-5}	4.8231	4.30223×10^{-6}	4.9949	6.08057×10^{-6}	4.9933
128×128	9.01604×10^{-7}	5.0064	1.47194×10^{-6}	4.9659	1.34593×10^{-7}	4.9984	1.90308×10^{-7}	4.9978
256×256	2.80641×10^{-8}	5.0057	4.55154×10^{-8}	5.0152	4.21019×10^{-9}	4.9986	5.95384×10^{-9}	4.9984
	WENO-NIP				**WENO-NIP+**			
$N_x \times N_y$	L_2 **Error**	L_2 **Order**	L_∞ **Error**	L_∞ **Order**	L_2 **Error**	L_2 **Order**	L_∞ **Error**	L_∞ **Order**
32×32	1.36590×10^{-4}	-	1.91790×10^{-4}	-	1.36590×10^{-4}	-	1.91790×10^{-4}	-
64×64	4.30186×10^{-6}	4.9887	6.07712×10^{-6}	4.9800	4.30186×10^{-6}	4.9887	6.07712×10^{-6}	4.9800
128×128	1.34592×10^{-7}	4.9983	1.90302×10^{-7}	4.9970	1.34592×10^{-7}	4.9983	1.90302×10^{-7}	4.9970
256×256	4.21019×10^{-9}	4.9986	5.95383×10^{-9}	4.9983	4.21019×10^{-9}	4.9986	5.95383×10^{-9}	4.9983

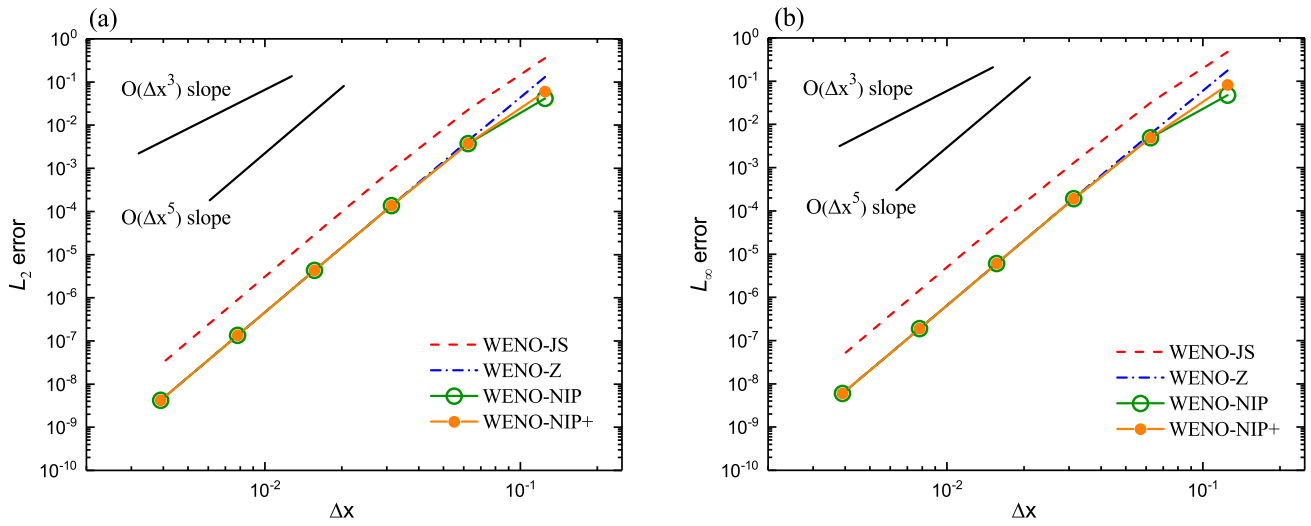

Figure 11. Plots of computing errors for different WENO schemes for Example 4: (**a**) L_2-norm error; (**b**) L_∞-norm error.

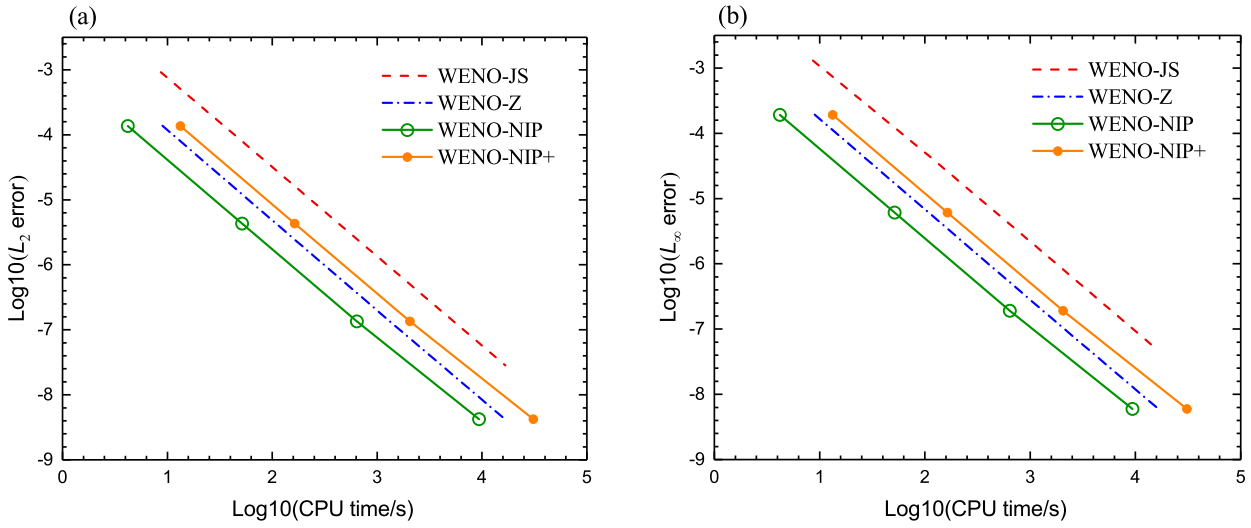

Figure 12. Comparison of various WENO schemes for Example 4 in CPU time and computing errors: (**a**) L_2-norm error; (**b**) L_∞-norm error.

Example 5. *We also compute the "oblique" linear advection problem but with a different initial condition. The problem is defined by*

$$\begin{cases} \dfrac{\partial C}{\partial t} + \dfrac{\partial C}{\partial x} + \dfrac{\partial C}{\partial y} = 0, & (x,y) \in [0,1] \times [0,1], t > 0, \\ C_0(x,y) = \sin\left[2\pi(x+y) - \dfrac{\sin\left(2\pi(x+y)\right)}{2\pi}\right], & (x,y) \in [0,1] \times [0,1], t = 0. \end{cases} \tag{15}$$

In addition, the periodic boundary condition is used, and the CFL number is taken to be $h^{2/3}$. *We know that the exact solution to Equation* (15) *is simply* $C(x,y,t) = \sin\Big(2\pi(x+y-2t) - \sin\left(2\pi(x+y-2t)\right)/2\pi\Big)$.

For this problem, we give the L_2- and L_∞-norm accuracy and orders of convergence of WENO-JS, WENO-Z, WENO-NIP, and WENO-NIP+ in Table 2. It can be found that the L_∞-norm convergence orders of WENO-JS decrease to third-order with refined meshes, and the L_∞-norm convergence orders drop to less than fourth-order accordingly. However, the WENO-NIP+ scheme and the associated WENO-NIP scheme can achieve the fifth-order convergence orders, and they still have almost the same accuracy. Similarly, we plot the overall L_2 and L_∞ convergence behavior of different schemes in Figure 13, and the slopes of the lines indicate that the solutions of WENO-NIP+ and WENO-NIP, as well as WENO-Z, converge at the optimal order, especially for slightly larger grid numbers. Clearly, Figure 13 illustrates that WENO-JS fails to recover the optimal convergence order for this test.

Table 2. Numerical errors and convergence orders of accuracy when solving Example 5, $t = 2.0$, CFL = $h^{2/3}$.

	WENO-JS				**WENO-Z**			
$N_x \times N_y$	L_2 **Error**	L_2 **Order**	L_∞ **Error**	L_∞ **Order**	L_2 **Error**	L_2 **Order**	L_∞ **Error**	L_∞ **Order**
32×32	2.03062×10^{-3}	-	4.04906×10^{-3}	-	6.86957×10^{-4}	-	1.34742×10^{-3}	-
64×64	1.01926×10^{-4}	4.3163	2.20372×10^{-4}	4.1996	2.30572×10^{-5}	4.8969	4.54011×10^{-5}	4.8913
128×128	5.18485×10^{-6}	4.2971	1.87594×10^{-5}	3.5543	7.28369×10^{-7}	4.9844	1.41758×10^{-6}	5.0012
256×256	3.34442×10^{-7}	3.9545	1.79724×10^{-6}	3.3838	2.28079×10^{-8}	4.9971	4.44483×10^{-8}	4.9952
	WENO-NIP				**WENO-NIP+**			
$N_x \times N_y$	L_2 **Error**	L_2 **Order**	L_∞ **Error**	L_∞ **Order**	L_2 **Error**	L_2 **Order**	L_∞ **Error**	L_∞ **Order**
32×32	7.11568×10^{-4}	-	1.36979×10^{-3}	-	7.11568×10^{-4}	-	1.36979×10^{-3}	-
64×64	2.31851×10^{-5}	4.9397	4.50977×10^{-5}	4.9248	2.31851×10^{-5}	4.9397	4.50977×10^{-5}	4.9248
128×128	7.28894×10^{-7}	4.9913	1.41780×10^{-6}	4.9913	7.28894×10^{-7}	4.9913	1.41780×10^{-6}	4.9913
256×256	2.28100×10^{-8}	4.9980	4.44482×10^{-8}	4.9954	2.28100×10^{-8}	4.9980	4.44482×10^{-8}	4.9954

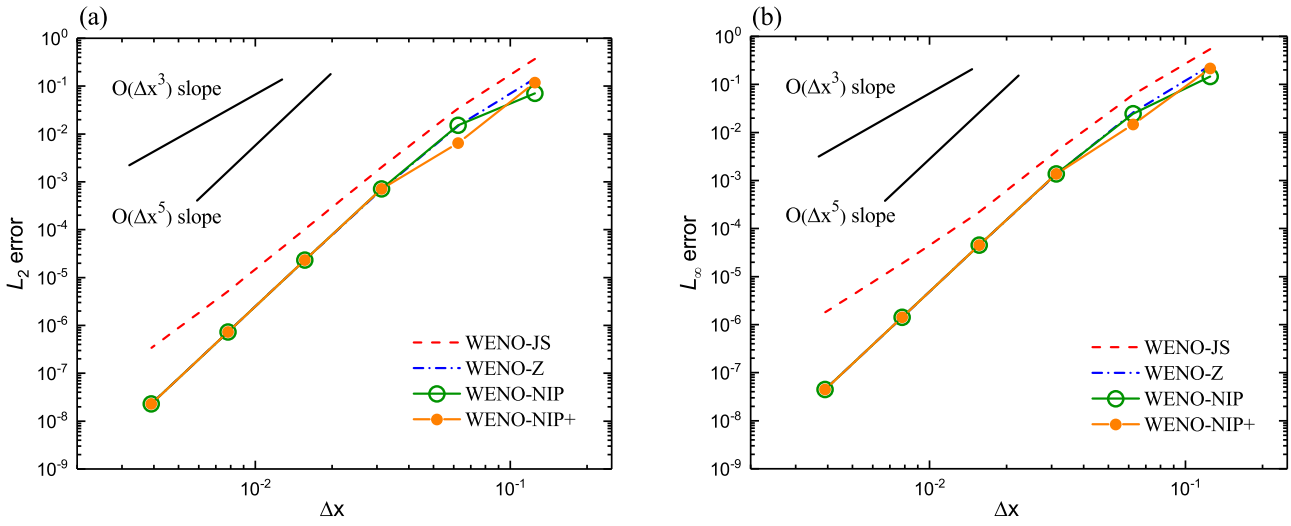

Figure 13. Plots of computing errors for different WENO schemes for Example 5: (**a**) L_2-norm error; (**b**) L_∞-norm error.

Similarly, we examine the CPU time consumed by different considered schemes for this test. As before, Figure 14 indicates that the WENO-NIP+ scheme has much better efficiency than the WENO-JS scheme, and its efficiency is lower than those of the WENO-Z and WENO-NIP schemes.

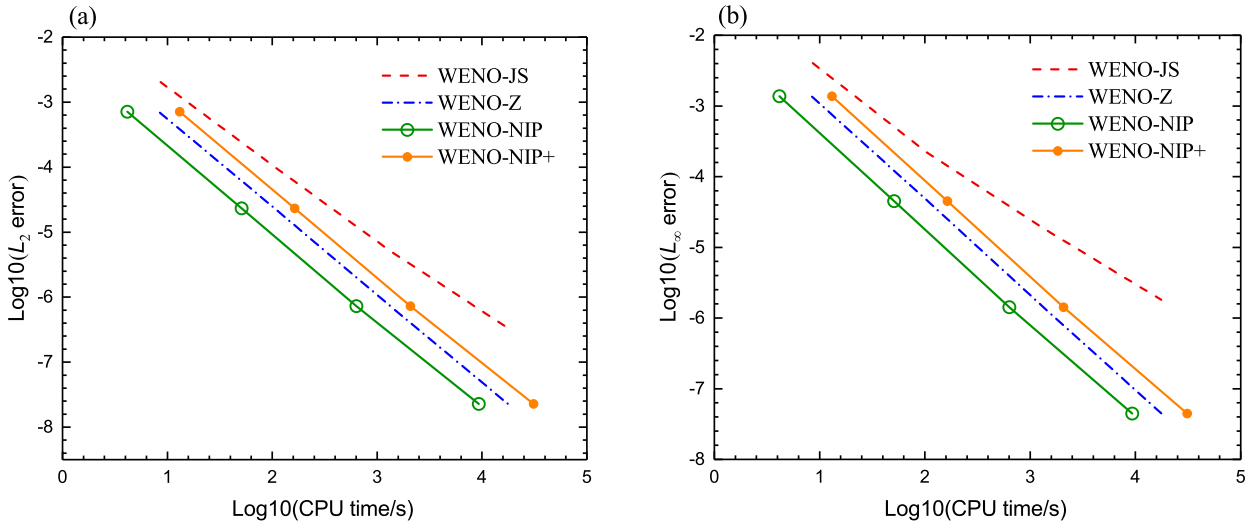

Figure 14. Comparison of various WENO schemes for Example 5 in CPU time and computing errors: (**a**) L_2-norm error; (**b**) L_∞-norm error.

5.2. 1D Euler Equations

The system of 1D Euler equations with strong conservative form is given as

$$\begin{aligned} &\frac{\partial \rho}{\partial t} + \frac{\partial (\rho u)}{\partial x} = 0, \\ &\frac{\partial (\rho u)}{\partial t} + \frac{\partial (\rho u^2 + p)}{\partial x} = 0, \\ &\frac{\partial E}{\partial t} + \frac{\partial (uE + up)}{\partial x} = 0, \end{aligned} \tag{16}$$

where ρ, u, p, E are the density, velocity, pressure, and total energy, respectively. Equation (16) is closed by the following equation of state:

$$E = \frac{p}{\gamma - 1} + \frac{1}{2}\rho u^2, \quad \gamma = 1.4.$$

Example 6. *We first compute the standard shock-tube problem of Sod [45]. Its initial condition is specified by*

$$(\rho, u, p)(x, 0) = \begin{cases} (1.0, 0.0, 1.0), & x \in [0.0, 0.5], \\ (0.125, 0.0, 0.1), & x \in [0.5, 1.0]. \end{cases}$$

At $x = 0$ and $x = 1$, the transmissive boundary conditions are used. The computation is advanced until $t = 0.25$.

Figure 15 presents the results of density profiles computed by WENO-JS, WENO-Z, WENO-NIP, and WENO-NIP+ with various uniform mesh cells of $N = 300, 900$. For simplicity, we only show the zoom near the discontinuity for the case of $N = 900$. By taking a close observation, we can find that WENO-NIP+, as well as WENO-JS and WENO-Z, can successfully avoid spurious oscillations. However, it can be seen that WENO-NIP produces evident spurious oscillations.

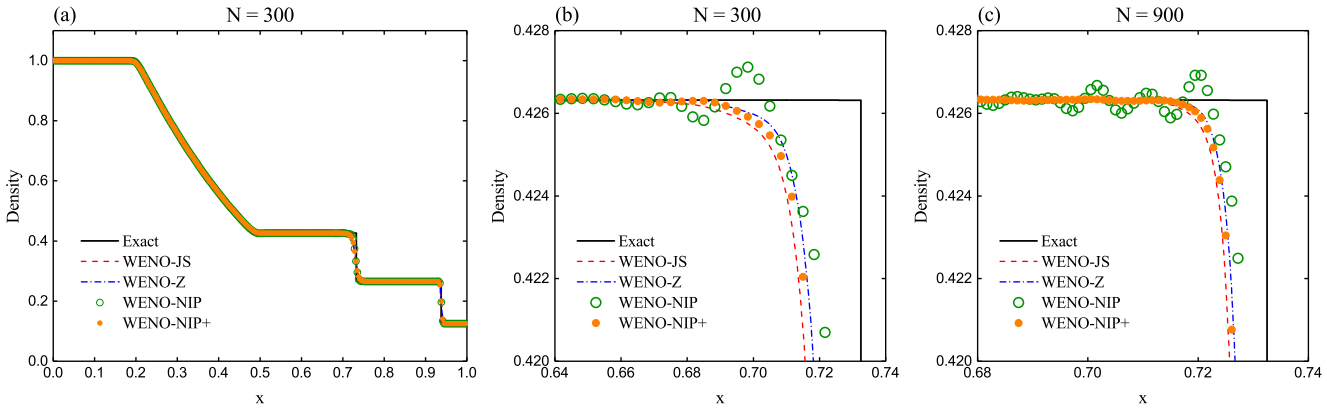

Figure 15. (**a**) Results of Sod's shock-tube problem computed by WENO-JS, WENO-Z, WENO-NIP, and WENO-NIP+ at $t = 0.25$ with $N = 300$. (**b**) Zoom in near the discontinuity with $N = 300$. (**c**) Zoom in near the discontinuity with $N = 900$.

Example 7. *Next, we compute the standard shock-tube problem of Lax [46]. Its initial condition is specified by*

$$(\rho, u, p)(x, 0) = \begin{cases} (0.445, 0.698, 3.528), & x \in [-5, 0], \\ (0.500, 0.000, 0.571), & x \in [0, 5]. \end{cases}$$

At $x = \pm 5$, the transmissive boundary conditions are used. The computation is advanced until $t = 1.3$.

The computed density profiles of WENO-JS, WENO-Z, WENO-NIP, and WENO-NIP+ with various uniform mesh cells of $N = 300, 900$ are shown in Figure 16. Again, we only show the zoom near the discontinuity for the case of $N = 900$. Similarly, we can observe that WENO-NIP generates unfavorable spurious oscillations, while WENO-NIP+ can successfully remove them. The WENO-JS and WENO-Z schemes can also avoid spurious oscillations, and they can perform as well as WENO-NIP+.

Example 8. *In this test, we solve the shock-density wave interaction of Shu and Osher [47]. The initial condition is given as*

$$(\rho, u, p)(x, 0) = \begin{cases} (3.857143, 2.629369, 10.333333), & x \in [-5.0, -4.0], \\ (1.0 + 0.2\sin(5x), 0, 1), & x \in [-4.0, 5.0]. \end{cases}$$

At $x = \pm 5$, the zero-gradient boundary conditions are used. The computation is advanced until $t = 1.8$, and the uniform cell number is chosen to be $N = 300$.

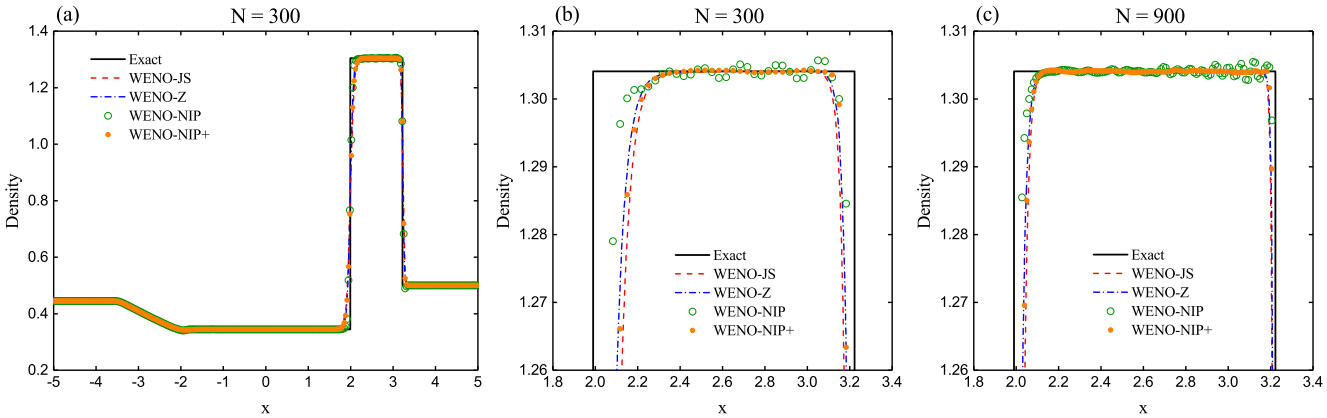

Figure 16. (**a**) Results of Lax's shock-tube problem computed by WENO-JS, WENO-Z, WENO-NIP, and WENO-NIP+ at $t = 1.3$ with $N = 300$. (**b**) Zoom in near the top with $N = 300$. (**c**) Zoom in near the top with $N = 900$.

In Figure 17, the solutions of the density computed by WENO-JS, WENO-Z, WENO-NIP, and WENO-NIP+ are plotted. The reference solution is obtained by using the WENO-JS scheme with a refined mesh of N = 10,000. It can be seen that WENO-NIP falsely amplifies the waves behind the high-frequency wave region, while WENO-NIP+ can properly prevent this false amplifications, as shown in Figure 17b. Clearly, the resolution of the high-frequency smooth waves of WENO-NIP+ is remarkably higher than those of WENO-JS and WENO-Z. It seems that the peaks of WENO-NIP are, to some extent, higher than those of the WENO-NIP+ solution. This is because WENO-NIP allows negative dissipation (see Figure 2d), but as discussed earlier, this is harmful to the stability of the scheme.

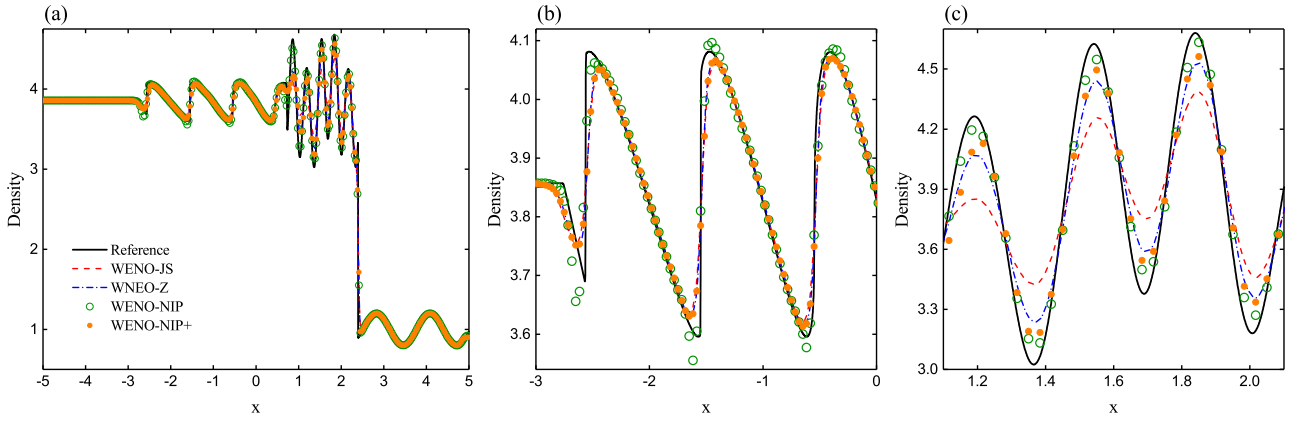

Figure 17. (**a**) Numerical solutions of the shock-density wave interaction of Shu and Osher calculated by WENO-JS, WENO-Z, WENO-NIP, and WENO-NIP+ at $t = 1.8$ with $N = 300$. (**b**) Zoom in near the region behind the high-frequency waves. (**c**) Zoom in near the high-frequency waves.

Example 9. *As a more severe version of the previous Shu–Osher shock-density wave interaction problem [47], this shock-density wave interaction of Titarev and Toro [48–50] is broadly taken to measure the ability to capture both shocks and short-wavelength oscillations of the numerical schemes. The computational domain is* $[-5.0, 5.0]$*, and it is initialized by*

$$(\rho, u, p)(x, 0) = \begin{cases} (1.515695, 0.523346, 1.805000), & x \in [-5.0, -4.5], \\ (1.0 + 0.1\sin(20\pi x), 0, 1), & x \in [-4.5, 5.0]. \end{cases}$$

At $x = \pm 5$*, the zero-gradient boundary conditions are used. The computation is advanced until* $t = 5.0$*, and the uniform cell number is chosen to be* $N = 1500$*.*

The computed results of the density of WENO-JS, WENO-Z, WENO-NIP, and WENO-NIP+ are presented in Figure 18, where the reference solution is obtained by WENO-JS with a refined mesh of N = 10,000. It can be found that the resolution of WENO-JS is lowest, and then that of WENO-Z. The resolution of WENO-NIP+ is much better than those of WENO-JS and WENO-Z. Actually, the resolution of the high-frequency smooth waves of WENO-NIP+ is almost identical to (see Figure 18c), or very close to (albeit very slightly lower, see Figure 18b), that of WENO-NIP.

Example 10. *In this final test of 1D Euler equations, we try to show the advantage of WENO-NIP+ with regard to decreasing numerical oscillations when solving hyperbolic conservation systems in the component-wise framework. To do this, we choose to calculate the Woodward–Colella interacting blast wave problem [51]. Its initial condition is given by*

$$(\rho, u, p)(x, 0) = \begin{cases} (1, 0, 1000), & x \in [0, 0.1), \\ (1, 0, 0.01), & x \in [0.1, 0.9), \\ (1, 0, 100), & x \in [0.9, 1.0]. \end{cases}$$

At $x = 0$ and $x = 1$, the reflective boundary conditions are used. It is run with $N = 600$ uniform cells until $t = 0.038$.

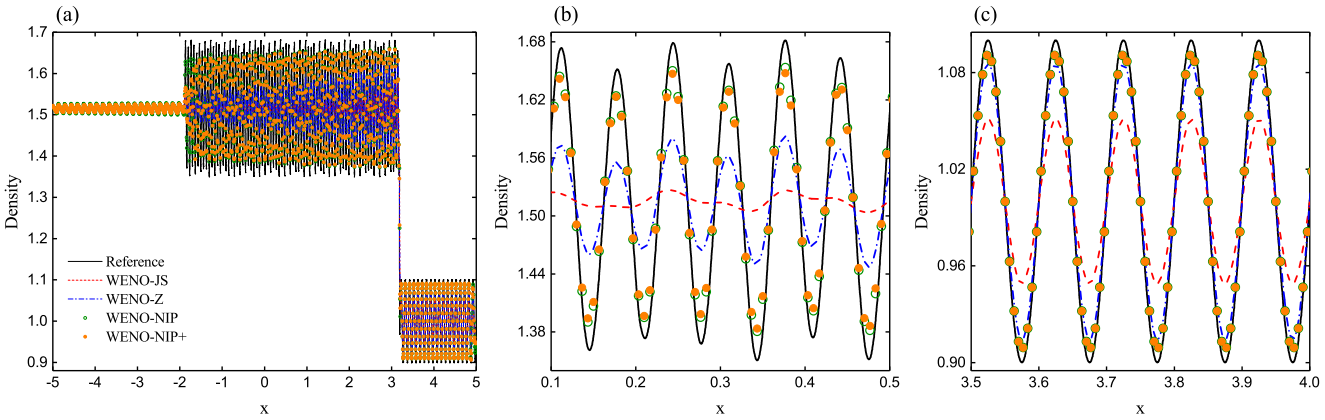

Figure 18. (**a**) Numerical solutions of the shock-density wave interaction of Titarev and Toro calculated by WENO-JS, WENO-Z, WENO-NIP, and WENO-NIP+ at $t = 5.0$ with $N = 1500$. (**b**) Zoomed-in view of the high-frequency waves. (**c**) Zoomed-in view of the region before the high-frequency waves.

Figure 19 plots the simulated density profiles of WENO-JS, WENO-Z, WENO-NIP, and WENO-NIP+. The reference solution is obtained by WENO-JS in the charateristic-wise framework with a refined uniform mesh of N = 10,000. It is evident that WENO-NIP generates severe spurious oscillations and falsely amplifies the solution. However, WENO-NIP+ almost removes the spurious oscillations and avoids the false amplification successfully. Furthermore, it appears that WENO-NIP+ performs slightly better than WENO-JS and WENO-Z for this test.

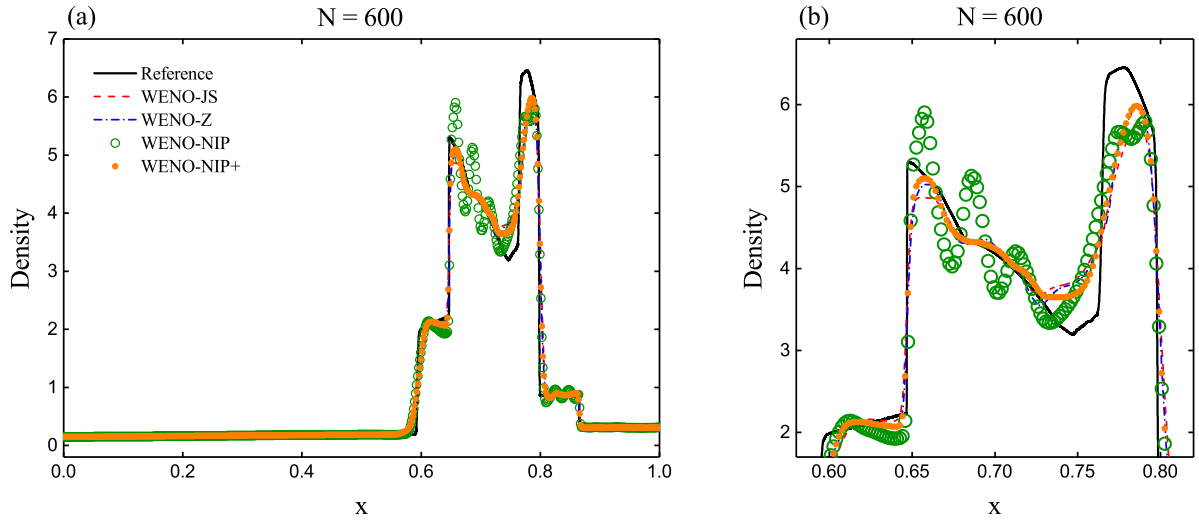

Figure 19. (**a**) Numerical solutions of the interacting blast wave problem calculated by WENO-JS, WENO-Z, WENO-NIP, and WENO-NIP+ in component-wise framework at $t = 0.038$ with $N = 600$. (**b**) Zoomed-in view of the interacting region.

5.3. 2D Euler Equations

The system of 2D Euler equations with strong conservative form is given as

$$\begin{aligned}
&\frac{\partial \rho}{\partial t}+\frac{\partial(\rho u)}{\partial x}+\frac{\partial(\rho v)}{\partial y}=0,\\
&\frac{\partial(\rho u)}{\partial t}+\frac{\partial(\rho u^2+p)}{\partial x}+\frac{\partial(\rho u v)}{\partial y}=0,\\
&\frac{\partial(\rho v)}{\partial t}+\frac{\partial(\rho v u)}{\partial x}+\frac{\partial(\rho v^2+p)}{\partial y}=0,\\
&\frac{\partial E}{\partial t}+\frac{\partial(u E+u p)}{\partial x}+\frac{\partial(v E+v p)}{\partial y}=0,
\end{aligned} \tag{17}$$

where y, v are the other direction and the velocity component in this direction, respectively. Equation (17) is closed by the following equation of state:

$$E=\frac{p}{\gamma-1}+\frac{1}{2}\rho\left(u^2+v^2\right),$$

Unless indicated otherwise, γ is chosen to be 1.4.

Example 11. *We first simulate the 2D shock-density wave interaction of Titarev and Toro. Its initial condition is given as*

$$(\rho,u,v,p)(x,y,0)=\begin{cases}(1.515695,0.523346,0,1.805000), & x\in[-5,-4.5),\\ \left(1.0+0.1\sin\left(20\pi x\cos\frac{\pi}{6}+20\pi y\sin\frac{\pi}{6}\right),0,0,1\right), & x\in[-4.5,5],\end{cases}$$

with the initial sine waves making an angle of $\pi/6$ in the $x\times y$ plane. At $x=\pm 5$, the transmissive boundary conditions are used, and at the top and bottom boundaries, the periodic conditions are used. The output time is set to be $t=5.0$, and a uniform mesh size of $N_x\times N_y=1500\times 300$ is taken.

In Figures 20 and 21, we present the density contours and the cross-sectional slices of density plot along the plane $y=0.0$ of the WENO-JS, WENO-Z, WENO-NIP, and WENO-NIP+ schemes, respectively. It can be found that WENO-JS gives the lowest resolution, and WENO-Z gives the second-lowest resolution. Figure 21b indicates that WENO-NIP falsely amplifies the solution behind the region of the high-frequency wave, while WENO-NIP+ can fix this problem. Moreover, as shown in Figure 21c, the peaks of the high-frequency waves of the WENO-NIP+ solution are, to some extent, higher than those of the WENO-NIP solution, albeit on a small scale. As expected, the peaks of the high-frequency waves of both the WENO-NIP+ and WENO-NIP solutions are significantly higher than those of the WENO-JS and WENO-Z solutions.

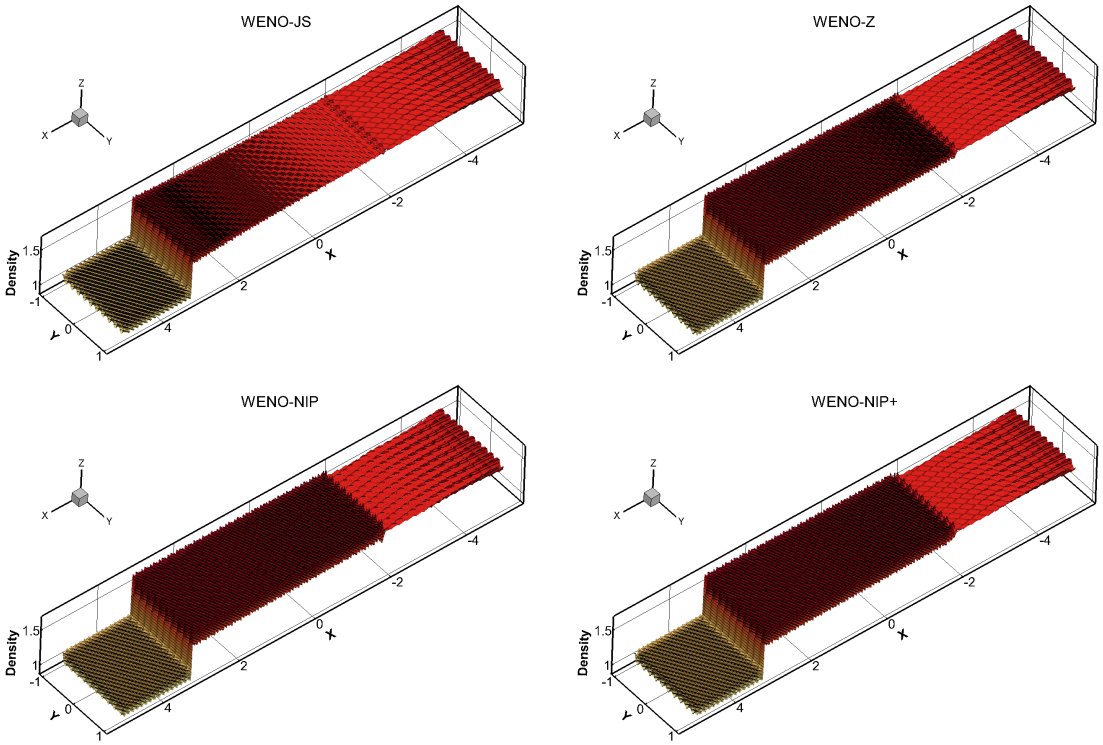

Figure 20. Numerical solutions of the 2D shock-density wave interaction of Titarev and Toro using 1500×300 cells at $t = 5.0$. Left upper corner, WENO-JS. Right upper corner, WENO-Z. Left lower corner, WENO-NIP. Right lower corner, WENO-NIP+.

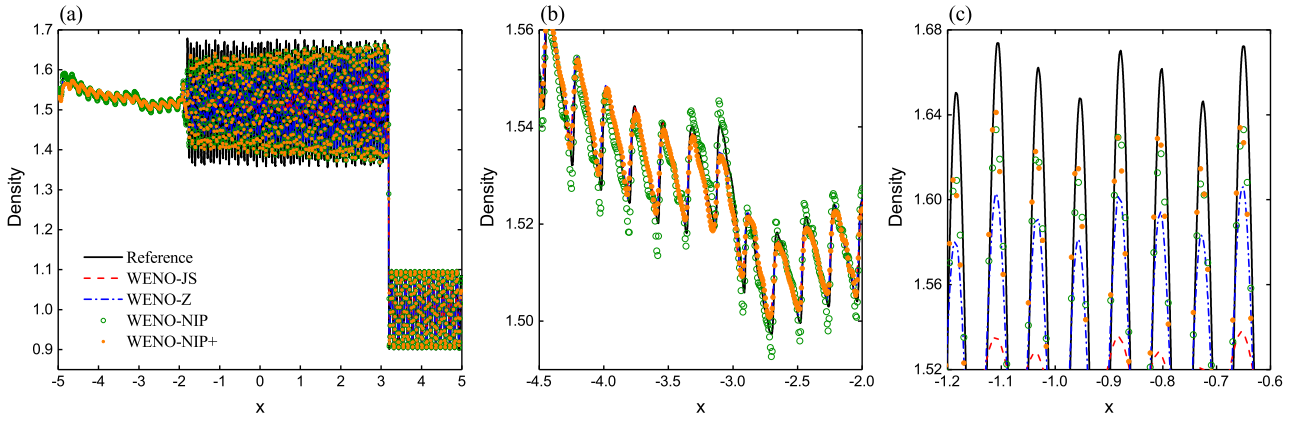

Figure 21. (**a**) The cross-sectional slices of density plot along the plane $y = 0.0$ for the 2D shock-density wave interaction of Titarev and Toro. (**b**) Zoom in near the region behind the high-frequency waves. (**c**) Zoom in near the high-frequency waves.

Example 12. *Next, we simulate the famous 2D Riemann problem [52–54]. Lax et al. [54] classified a total of 19 genuinely different configurations for the 2D Riemann problem, and we consider Configuration 4 here for the test. The computational domain* $[0,1] \times [0,1]$ *is initialized by*

$$(\rho, u, v, p)(x, y, 0) = \begin{cases} (1.1, 0.0, 0.0, 1.1), & 0.5 \le x \le 1.0, 0.5 \le y \le 1.0, \\ (0.5065, 0.8939, 0.0, 0.35), & 0.0 \le x \le 0.5, 0.5 \le y \le 1.0, \\ (1.1, 0.8939, 0.8939, 1.1), & 0.0 \le x \le 0.5, 0.0 \le y \le 0.5, \\ (0.5065, 0.0, 0.8939, 0.35), & 0.5 \le x \le 1.0, 0.0 \le y \le 0.5. \end{cases}$$

On all boundaries, the transmission boundary condition is used. We perform the numerical calculations on a uniform mesh size of 800×800*, and all the computations proceed to* $t = 0.25$.

Figure 22 shows the density contours of the WENO-JS, WENO-Z, WENO-NIP, and WENO-NIP+ schemes. It is clear that all these schemes can properly capture the main structure of the complicated flow field. However, we can observe that there are obvious post-shock oscillations (see Figure 22), which are unfavorable for the fidelity of the results, in the solution of the WENO-NIP scheme. Noticeably, these oscillations have been removed or greatly decreased by the WENO-NIP+ scheme. The WENO-JS and WENO-Z schemes can also control the oscillations successfully.

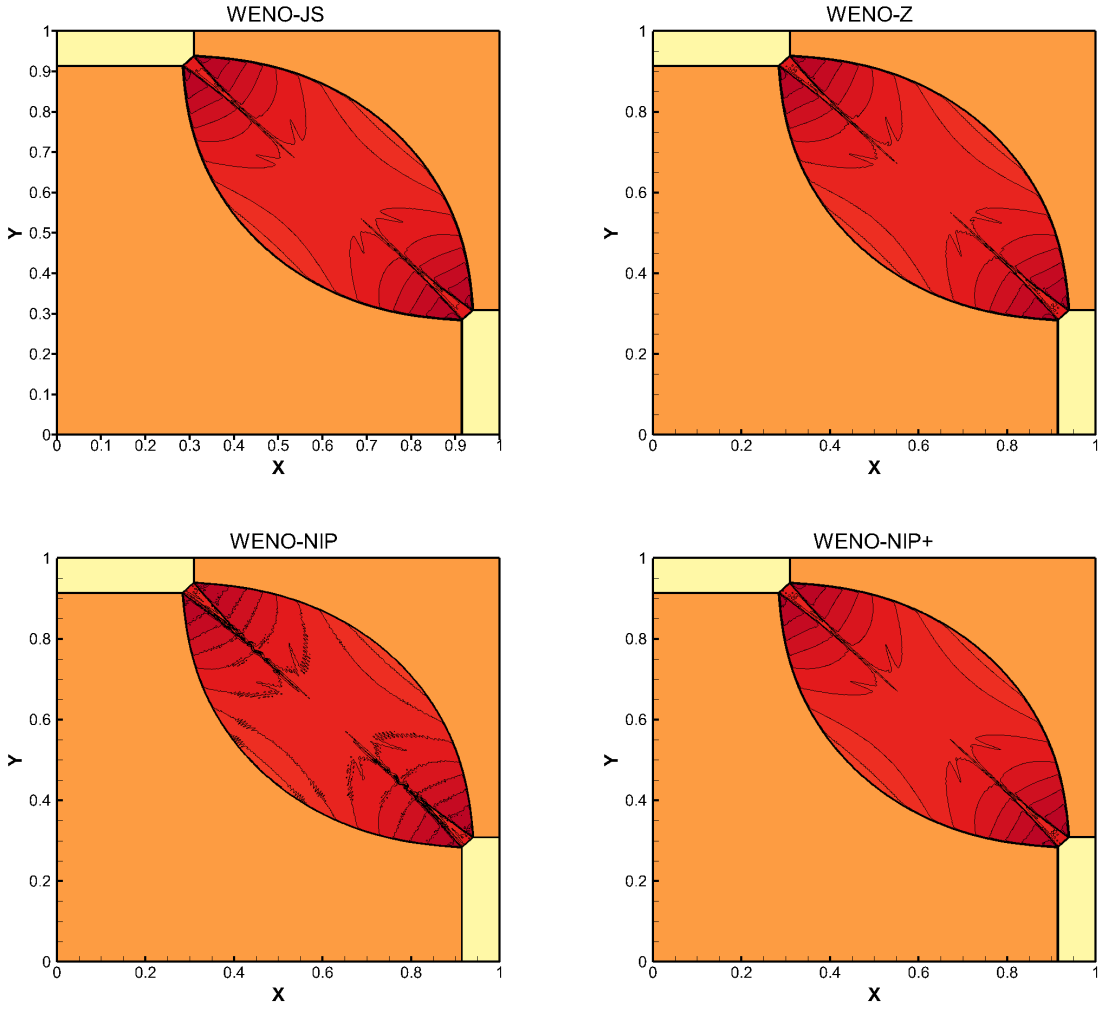

Figure 22. Numerical solutions of the 2D Riemann problem using 800×800 cells at $t = 0.25$. Left upper corner, WENO-JS. Right upper corner, WENO-Z. Left lower corner, WENO-NIP. Right lower corner, WENO-NIP+.

Example 13. *The shock-vortex interaction problem [55,56] is a well-known 2D test for high-resolution schemes. The initial condition is given as*

$$(\rho, u, v, p)(x, y, 0) = \begin{cases} \boldsymbol{U}_{\mathrm{L}}, & x < 0.5, \\ \boldsymbol{U}_{\mathrm{R}}, & x \geq 0.5, \end{cases}$$

where $\boldsymbol{U}_{\mathrm{L}} = (\rho_{\mathrm{L}}, u_{\mathrm{L}}, v_{\mathrm{L}}, p_{\mathrm{L}}) = (1, \sqrt{\gamma}, 0, 1)$, *and* $\boldsymbol{U}_{\mathrm{R}} = (\rho_{\mathrm{R}}, u_{\mathrm{R}}, v_{\mathrm{R}}, p_{\mathrm{R}})$, *taking the form*

$$p_{\mathrm{R}} = 1.3, \rho_{\mathrm{R}} = \rho_{\mathrm{L}}\left(\frac{\gamma - 1 + (\gamma + 1)p_{\mathrm{R}}}{\gamma + 1 + (\gamma - 1)p_{\mathrm{R}}}\right), u_{\mathrm{R}} = u_{\mathrm{L}}\left(\frac{1 - p_{\mathrm{R}}}{\sqrt{\gamma - 1 + p_{\mathrm{R}}(\gamma + 1)}}\right), v_{\mathrm{R}} = 0.$$

The following vortex $\delta \boldsymbol{U}$ defined by perturbations is superimposed onto the left state $\boldsymbol{U}_{\mathrm{L}}$,

$$\delta \boldsymbol{U} = (\delta\rho, \delta u, \delta v, \delta p) = \left(\frac{\rho_{\mathrm{L}}^2}{(\gamma-1)p_{\mathrm{L}}}\delta T, \epsilon \frac{y-y_{\mathrm{c}}}{r_{\mathrm{c}}} \mathrm{e}^{\alpha(1-r^2)}, -\epsilon \frac{x-x_{\mathrm{c}}}{r_{\mathrm{c}}} \mathrm{e}^{\alpha(1-r^2)}, \frac{\gamma\rho_{\mathrm{L}}^2}{(\gamma-1)\rho_{\mathrm{L}}}\delta T \right),$$

where $\epsilon = 0.3, r_{\mathrm{c}} = 0.05, \alpha = 0.204, x_{\mathrm{c}} = 0.25, y_{\mathrm{c}} = 0.5, r = \sqrt{((x-x_{\mathrm{c}})^2 + (y-y_{\mathrm{c}})^2)/r_{\mathrm{c}}^2}$, $\delta T = -(\gamma-1)\epsilon^2 \mathrm{e}^{2\alpha(1-r^2)}/(4\alpha\gamma)$. On all boundaries, the transmissive boundary condition is used. We perform the simulations until $t = 0.6$ by using a uniform mesh size of 800×800.

The computed density contours of the WENO-JS, WENO-Z, WENO-NIP, and WENO-NIP+ schemes are plotted in Figure 23. As before, WENO-NIP+, as well as WENO-JS and WENO-Z, can capture the main structure of the complicated flow field properly. However, it is clear that WENO-NIP produces very severe numerical oscillations. Moreover, careful examination (see the last column of Figure 23) indicates that WENO-NIP+ is less oscillatory than WENO-Z, albeit very slightly.

Example 14. *In the final numerical test, we consider the regular shock reflection, which was simulated carefully in [57]. For this typical 2D steady flow, the computational domain of $[0,4] \times [0,1]$ is initialized by*

$$(\rho, u, v, p)(x, y, 0) = (1.0, 2.9, 0.0, 1.0/\gamma).$$

At the bottom and right boundaries, the reflection and transmissive boundary conditions are used, respectively. At the top and left boundaries, the following Dirichlet boundary conditions are specified:

$$(\rho, u, v, p)(x, y, t) = \begin{cases} (1.69997, 2.61934, -0.50632, 1.52819), & \text{where} \quad y = 1, \\ (1.0, 2.9, 0.0, 1.0/\gamma), & \text{where} \quad x = 0. \end{cases}$$

The computation proceeds to $t = 2.5$, and a uniform mesh size of 800×200 is taken.

The density contours computed by WENO-JS, WENO-Z, WENO-NIP, and WENO-NIP+ are presented in Figure 24. Generally speaking, all the considered schemes can capture the main structure of the shock transitions for this problem. Clearly, the post-shock numerical oscillations can be observed for all considered schemes. However, compared to WENO-NIP, which generates very severe numerical oscillations, WENO-NIP+ can significantly decrease these oscillations. To manifest this further, we plot the cross-sectional slices of the density of WENO-NIP and WENO-NIP+ along the plane $y = 0.5$ over $x \in (0.9, 1.1)$ in Figure 25. For the purpose of comparison, the results of WENO-ZS [57] using two different mesh sizes of $N_x \times N_y = 800 \times 200, 1600 \times 400$ are also plotted. It was demonstrated carefully that WENO-ZS is able to either remove or significantly reduce the post-shock oscillations successfully. Obviously, the post-shock oscillations produced by WENO-NIP are far more severe than that of WENO-NIP+. In other words, the post-shock oscillations of WENO-NIP+ are considerably reduced compared to those of WENO-NIP. We conclude that this should be an advantage of WENO-NIP+. In addition, although the post-shock oscillations generated by WENO-NIP+ are slightly more severe than those of WENO-ZS, WENO-NIP+ achieves higher resolutions than WENO-ZS under the same mesh resolution. Indeed, the resolution of WENO-NIP+ with $N_x \times N_y = 800 \times 200$ is comparable to that of WENO-ZS with $N_x \times N_y = 1600 \times 400$. In summary, this might be another advantage of WENO-NIP+ in some ways.

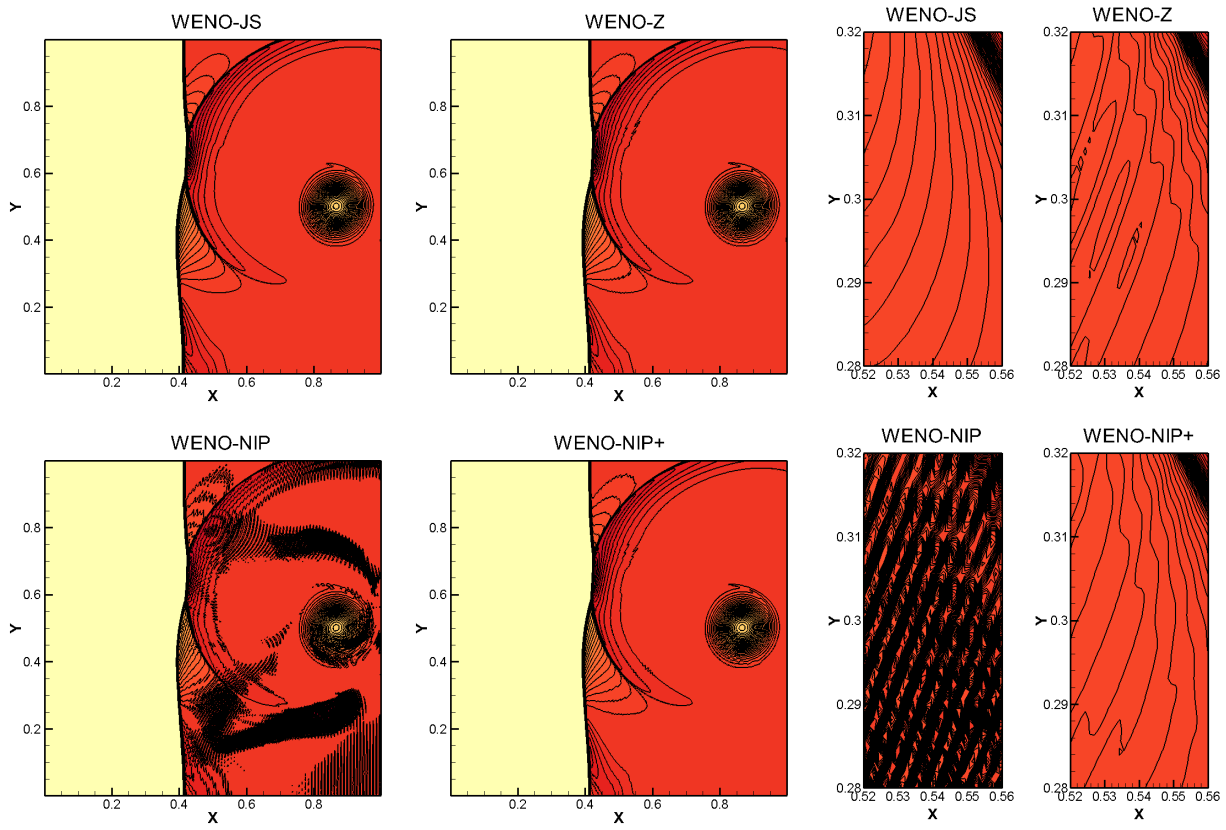

Figure 23. Numerical solutions of the shock-vortex interaction problem using 800×800 cells at $t = 0.60$. Left upper corner of the first two columns, WENO-JS. Right upper corner of the first two columns, WENO-Z. Left lower corner of the first two columns, WENO-NIP. Right lower corner of the first two columns, WENO-NIP+. Left upper corner of the last two columns, zoomed-in view of WENO-JS. Right upper corner of the last two columns, zoomed-in view of WENO-Z. Left lower corner of the last two columns, zoomed-in view of WENO-NIP. Right lower corner of the last two columns, zoomed-in view of WENO-NIP+.

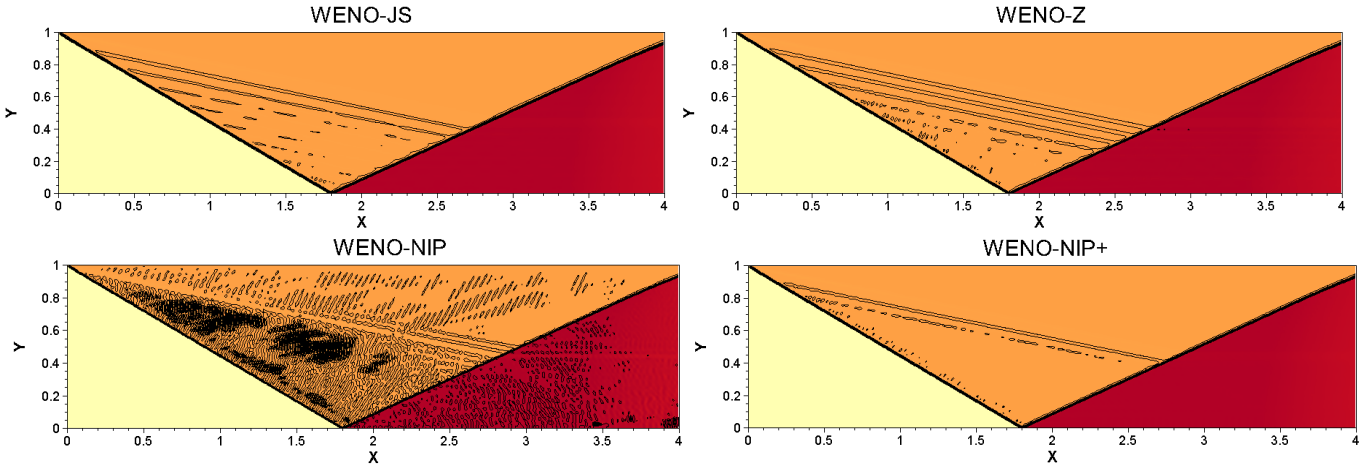

Figure 24. Density contours of the regular shock reflection of WENO-JS, WENO-Z, WENO-NIP, and WENO-NIP+ using 30 contour lines with a range from 1.05 to 2.7. Left upper corner, WENO-JS. Right upper corner, WENO-Z. Left lower corner, WENO-NIP. Right lower corner, WENO-NIP+.

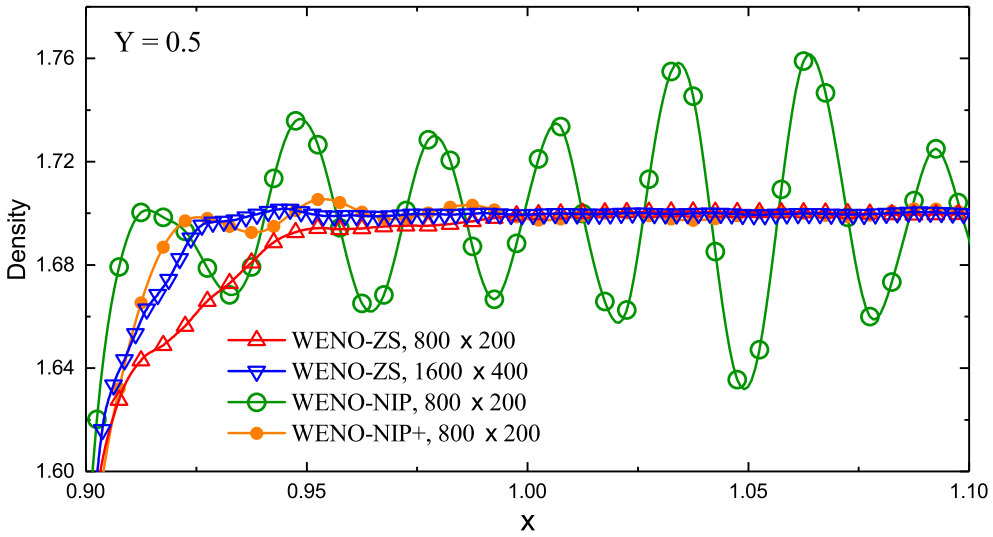

Figure 25. The cross-sectional slices of density plot of WENO-JS, WENO-Z, WENO-NIP, and WENO-NIP+ along the plane $y = 0.5$, where $x \in [0.9, 1.1]$.

6. Conclusions

It is the negative dissipation property that hinders improving the stability of the WENO-NIP scheme. This is the reason why WENO-NIP produces spurious oscillations for simulating problems with shocks or other discontinuities. Therefore, we propose a method of enhancing the WENO-NIP scheme by adding a new term in the weights formula of WENO-NIP to eliminate the negative dissipation. Numerical experiments demonstrate that the performance of the proposed scheme, dubbed WENO-NIP+, is greatly improved. It was numerically verified that WENO-NIP+ can obtain optimal convergence orders in smooth regions regardless of critical points. For long-run simulations of 1D linear advection problems with discontinuities, WENO-NIP+ can successfully avoid the spurious oscillations that are generated by WENO-NIP. Similarly, for simulations of 1D shock-tube problems, WENO-NIP+ properly prevents the spurious oscillations, while WENO-NIP does not. Furthermore, the proposed scheme is able to achieve comparable or even better results than WENO-NIP, WENO-JS, and WENO-Z in the regions with high-frequency smooth waves, like the shock-density wave interaction of Shu and Oser, and Titarev and Toro. Besides, it was demonstrated that WENO-NIP+ shows better performances than WENO-NIP when simulating 2D Euler equations with strong shock waves, and it can remove or noticeably decrease the post-shock oscillations. It should be pointed out that the proposed WENO-NIP+ scheme can achieve better performance in reducing oscillations, but at the price of higher computational cost, albeit not beyond an acceptable level.

Author Contributions: W.Z., conceptualization, methodology, programming, formal analysis, writing—original draft preparation, visualization, validation; R.L., supervision, writing—review and editing, data curation, validation. All authors have read and agreed to the published version of the manuscript.

Funding: This research received no external funding.

Data Availability Statement: Not applicable.

Conflicts of Interest: The authors declare no conflict of interest.

References

1. Liu, X.D.; Osher, S.; Chan, T. Weighted essentially non-oscillatory schemes. *J. Comput. Phys.* **1994**, *115*, 200–212. [CrossRef]
2. Jiang, G.S.; Shu, C.W. Efficient implementation of weighted ENO schemes. *J. Comput. Phys.* **1996**, *126*, 202–228. [CrossRef]
3. Shu, C.W. *Advanced Numerical Approximation of Nonlinear Hyperbolic Equations*; Lecture Notes in Mathematics; Springer: Berlin, Germany, 1998; pp. 325–432.
4. Li, R.; Zhong, W. A new mapped WENO scheme using order-preserving mapping. *Commun. Comput. Phys.* **2022**, *31*, 548–592.

5. Feng, H.; Hu, F.; Wang, R. A new mapped weighted essentially non-oscillatory scheme. *J. Sci. Comput.* **2012**, *51*, 449–473.
6. Li, Q.; Liu, P.; Zhang, H. Piecewise Polynomial Mapping Method and Corresponding WENO Scheme with Improved Resolution. *Commun. Comput. Phys.* **2015**, *18*, 1417–1444. [CrossRef]
7. Li, R.; Zhong, W. A modified adaptive improved mapped WENO method. *Commun. Comput. Phys.* **2021**, *30*, 1545–1588.
8. Li, R.; Zhong, W. An efficient mapped WENO scheme using approximate constant mapping. *Numer. Math. Theor. Meth. Appl.* **2022**, *15*, 1–41.
9. Yuan, M. A new weighted essentially non-oscillatory WENO-NIP scheme for hyperbolic conservation laws. *Comput. Fluids* **2020**, *197*, 104168. [CrossRef]
10. Henrick, A.K.; Aslam, T.D.; Powers, J.M. Mapped weighted essentially non-oscillatory schemes: Achieving optimal order near critical points. *J. Comput. Phys.* **2005**, *207*, 542–567. [CrossRef]
11. Borges, R.; Carmona, M.; Costa, B.; Don, W.S. An improved weighted essentially non-oscillatory scheme for hyperbolic conservation laws. *J. Comput. Phys.* **2008**, *227*, 3191–3211.
12. Feng, H.; Huang, C.; Wang, R. An improved mapped weighted essentially non-oscillatory scheme. *Appl. Math. Comput.* **2014**, *232*, 453–468. [CrossRef]
13. Kossaczka, T.; Ehrhardt, M.; Gunther, M. A neural network enhanced weighted essentially non-oscillatory method for nonlinear degenerate parabolic equations. *Phys. Fluids* **2022**, *34*, 026604. [CrossRef]
14. Diaz-Adame, R.; Jerez, S.; Carrillo, H. Fast and Optimal WENO Schemes for Degenerate Parabolic Conservation Laws. *J. Sci. Comput.* **2022**, *90*, 22. [CrossRef]
15. Lin, J.; Xu, Y.; Xue, H.; Zhong, X. High Order Finite Difference WENO Methods with Unequal-Sized Sub-Stencils for the Degasperis-Procesi Type Equations. *Commun. Comput. Phys.* **2022**, *31*, 913–946. [CrossRef]
16. Zhou, X.; Zhong, C.; Li, Z.; Li, F. Preconditioned Jacobian-free NewtoneKrylov fully implicit high order WENO schemes and flux limiter methods for two-phase flow models. *Nucl. Eng. Technol.* **2022**, *54*, 49–60. [CrossRef]
17. Dumbser, M.; Kaser, M. Arbitrary high order non-oscillatory finite volume schemes on unstructured meshes for linear hyperbolic systems. *J. Comput. Phys.* **2007**, *221*, 693–723. [CrossRef]
18. Zhong, X.; Shu, C.W. A simple weighted essentially nonoscillatory limiter for Runge–Kutta discontinuous Galerkin methods. *J. Comput. Phys.* **2013**, *232*, 397–415. [CrossRef]
19. Pedro, J.C.; Banda, M.K.; Sibanda, P. On one-dimensional arbitrary high-order WENO schemes for systems of hyperbolic conservation laws. *Comp. Appl. Math.* **2014**, *33*, 363–384. [CrossRef]
20. Zhu, J.; Zhong, X.; Shu, C.W.; Qiu, J. Runge-Kutta Discontinuous Galerkin Method with a Simple and Compact Hermite WENO Limiter on Unstructured Meshes. *Commun. Comput. Phys.* **2017**, *21*, 623–649. [CrossRef]
21. Harten, A.; Engquist, B.; Osher, S.; Chakravarthy, S.R. Uniformly high order accurate essentially non-oscillatory schemes III. *J. Comput. Phys.* **1987**, *71*, 231–303. [CrossRef]
22. Harten, A.; Osher, S. Uniformly high order accurate essentially non-oscillatory schemes I. *SIAM J. Numer. Anal.* **1987**, *24*, 279–309. [CrossRef]
23. Harten, A.; Osher, S.; Engquist, B.; Chakravarthy, S.R. Some results on uniformly high order accurate essentially non-oscillatory schemes. *Appl. Numer. Math.* **1986**, *2*, 347–377. [CrossRef]
24. Harten, A. ENO schemes with subcell resolution. *J. Comput. Phys.* **1989**, *83*, 148–184. [CrossRef]
25. Li, R.; Zhong, W. Towards building the OP-Mapped WENO schemes: A general methodology. *Math. Comput. Appl.* **2021**, *26*, 67. [CrossRef]
26. Wang, R.; Feng, H.; Huang, C. A New Mapped Weighted Essentially Non-oscillatory Method Using Rational Function. *J. Sci. Comput.* **2016**, *67*, 540–580. [CrossRef]
27. Hong, Z.; Ye, Z.; Meng, X. A mapping-function-free WENO-M scheme with low computational cost. *J. Comput. Phys.* **2020**, *405*, 109145. [CrossRef]
28. Shu, C.W.; Osher, S. Efficient implementation of essentially non-oscillatory shock-capturing schemes. *J. Comput. Phys.* **1988**, *77*, 439–471. [CrossRef]
29. Gottlieb, S.; Shu, C.W.; Tadmor, E. Strong stability-preserving high-order time discretization methods. *SIAM Rev.* **2001**, *43*, 89–112. [CrossRef]
30. Gottlieb, S.; Shu, C.W. Total variation diminishing Runge-Kutta schemes. *Math. Comput.* **1998**, *67*, 73–85. [CrossRef]
31. Titarev, V.A.; Toro, E.F. ADER: Arbitrary high order Godunov approach. *J. Sci. Comput.* **2002**, *17*, 609–618. [CrossRef]
32. Titarev, V.A.; Toro, E.F. High order ADER schemes for the scalar advection-reaction-diffusion equations. *CFD J.* **2003**, *12*, 1–6.
33. Titarev, V.A.; Toro, E.F. ADER schemes for three-dimensional non-linear hyperbolic systems. *J. Comput. Phys.* **2005**, *204*, 715–736. [CrossRef]
34. Balsara, D.; Rumpf, T.; Dumbser, M.; Munz, C.D. Efficient, high accuracy ADER-WENO schemes for hydrodynamics and divergence-free magnetohydrodynamics. *J. Comput. Phys.* **2009**, *228*, 2480–2516. [CrossRef]
35. Dumbser, M.; Zanotti, O.; Hidalgo, A.; Balsara, D.S. ADER-WENO finite volume schemes with space-time adaptive mesh refinement. *J. Comput. Phys.* **2013**, *248*, 257–286. [CrossRef]
36. Boscheri, W.; Balsara, D.S.; Dumbser, M. Lagrangian ADER-WENO finite volume schemes on unstructured triangular meshes based on genuinely multidimensional HLL Riemann solvers. *J. Comput. Phys.* **2014**, *267*, 112–138. [CrossRef]

37. Dumbser, M.; Hidalgo, A.; Zanotti, O. High order space-time adaptive ADER-WENO finite volume schemes for non-conservative hyperbolic systems. *Comput. Meth. Appl. Mech. Eng.* **2014**, *268*, 359–387. [CrossRef]
38. Dumbser, M. Arbitrary-Lagrangian-Eulerian ADER-WENO finite volume schemes with time-accurate local time stepping for hyperbolic conservation laws. *Comput. Meth. Appl. Mech. Eng.* **2014**, *280*, 57–83. [CrossRef]
39. Avesani, D.; Dumbser, M.; Vacondio, R.; Righetti, M. An alternative SPH formulation: ADER-WENO-SPH. *Comput. Meth. Appl. Mech. Eng.* **2021**, *382*, 113871. [CrossRef]
40. Pirozzoli, S. On the spectral properties of shock-capturing schemes. *J. Comput. Phys.* **2006**, *219*, 489–497. [CrossRef]
41. Yamaleev, N.K.; Carpenter, M.H. A systematic methodology for constructing high-order energy stable WENO schemes. *J. Comput. Phys.* **2009**, *228*, 4248–4272. [CrossRef]
42. Fu, L.; Hu, X.Y.; Adams, N.A. A family of high-order targeted ENO schemes for compressible-fluid simulations. *J. Comput. Phys.* **2016**, *305*, 333–359. [CrossRef]
43. Jung, C.Y.; Nguyen, T.B. A new adaptive weighted essentially non-oscillatory WENO-θ scheme for hyperbolic conservation laws. *J. Comput. Appl. Math.* **2018**, *328*, 314–339. [CrossRef]
44. Christov, I.; Popov, B. New non-oscillatory central schemes on unstructured triangulations for hyperbolic systems of conservation laws. *J. Comput. Phys.* **2008**, *227*, 5736–5757. [CrossRef]
45. Sod, G.A. A survey of several finite difference methods for systems of nonlinear hyperbolic conservation laws. *J. Comput. Phys.* **1978**, *27*, 1–31. [CrossRef]
46. Lax, P.D. Weak solutions of nonlinear hyperbolic equations and their numerical computation. *Commun. Pure Appl. Math.* **1954**, *7*, 159–193. [CrossRef]
47. Shu, C.W.; Osher, S. Efficient implementation of essentially non-oscillatory shock-capturing schemes II. *J. Comput. Phys.* **1989**, *83*, 32–78. [CrossRef]
48. Titarev, V.A.; Toro, E.F. Finite-volume WENO schemes for three-dimensional conservation laws. *J. Comput. Phys.* **2004**, *201*, 238–260. [CrossRef]
49. Toro, E.F.; Titarev, V.A. TVD Fluxes for the High-Order ADER Schemes. *J. Sci. Comput.* **2005**, *24*, 285–309. [CrossRef]
50. Titarev, V.A.; Toro, E.F. WENO schemes based on upwind and centred TVD fluxes. *Comput. Fluids* **2005**, *34*, 705–720. [CrossRef]
51. Woodward, P.; Colella, P. The numerical simulation of two-dimensional fluid flow with strong shocks. *J. Comput. Phys.* **1984**, *54*, 115–173. [CrossRef]
52. Schulz-Rinne, C.W.; Collins, J.P.; Glaz, H.M. Numerical solution of the Riemann problem for two-dimensional gas dynamics. *SIAM J. Sci. Comput.* **1993**, *14*, 1394–1414. [CrossRef]
53. Schulz-Rinne, C.W. Classification of the Riemann problem for two-dimensional gas dynamics. *SIAM J. Math. Anal.* **1993**, *24*, 76–88. [CrossRef]
54. Lax, P.D.; Liu, X.D. Solution of two-dimensional Riemann problems of gas dynamics by positive schemes. *SIAM J. Sci. Comput.* **1998**, *19*, 319–340. [CrossRef]
55. Chatterjee, A. Shock wave deformation in shock-vortex interactions. *Shock Waves* **1999**, *9*, 95–105. [CrossRef]
56. Ren, Y.X.; Liu, M.; Zhang, H. A characteristic-wise hybrid compact-WENO scheme for solving hyperbolic conservation laws. *J. Comput. Phys.* **2003**, *192*, 365–386. [CrossRef]
57. Zhang, S.; Shu, C.W. A new smoothness indicator for the WENO schemes and its effect on the convergence to steady state solutions. *J. Sci. Comput.* **2007**, *31*, 273–305. [CrossRef]